PHYSICAL REVIEW E **104**, 044602 (2021)

Low-temperature ordering of the dimer phase of a two-dimensional model of core-softened particles

F. Mambretti,[1,2,*] M. Martinelli,[1] F. Civillini,[1] M. Bertoletti,[1] S. Riva,[1] N. Manini,[1] D. E. Galli,[1] and D. Pini[1]
[1]*Università degli Studi di Milano, Dipartimento di Fisica "Aldo Pontremoli," via Celoria 16, 20133 Milan, Italy*
[2]*Università degli Studi di Padova, Dipartimento di Fisica e Astronomia, via Marzolo 8, 35131 Padua, Italy*

(Received 3 August 2021; accepted 17 September 2021; published 7 October 2021)

Purely pairwise interactions of the core-softened type, i.e., featuring a soft repulsion followed by a hard-core interaction at shorter distance, give rise to nontrivial equilibrium structures entirely different from the standard close packing of spheres. In particular, in a suitable low-temperature region of their phase diagram, such interactions are well known to favor a transition from a fluid to a cluster crystal. The residual mutual interaction between individual clusters can lead to the formation of patterns of their reciprocal orientations. In this work, we investigate two examples of such models in two dimensions, at the density most appropriate to the dimer phase, whereby clusters consist of just two particles, studying them with optimization techniques and Monte Carlo simulations. We focus on the dimer crystal, and unveil a second phase transition at extremely low temperature. This transition leads from a triangular dimer lattice with randomly disordered dimer orientations at high temperature to a reduced-symmetry ground state with nematic orientational order and a slightly distorted structure characterized by a centered-rectangular lattice at low temperature.

DOI: 10.1103/PhysRevE.104.044602

I. INTRODUCTION

The broad range of structures observed in crystallography is usually ascribed to the variety of interatomic forces, with intricate dependences on mutual distances, angles, dihedrals, leading to different kinds of coordination [1]. In the realm of soft matter, however, one is faced with a different scenario: in that case, the effective interactions which arise between complex molecular systems when they are regarded as effective pointlike objects may behave very differently from those between their atomic counterparts, and even purely pairwise forces, which only depend on particle-particle distances, can give rise to nontrivial crystalline equilibrium structures different from the standard close packing of spheres (triangular lattice in two dimensions, face-centered cubic in three), which is the paradigm, e.g., for Lennard-Jones forces or for monodisperse hard spheres [2].

A remarkable instance of this behavior is found for the interactions variously referred to as core-corona or core-softened or hard-core–soft-shell potentials, such that a hard-core, singular repulsion is followed by a softer, bounded repulsion at larger distance. These potentials come along as a modelization of the effective interactions in several systems, such as colloidal particles coated by a polymer brush grafted to their surface [3–5], dendrimers [6], and block copolymer micelles [7–9]. The most popular example is the square-shoulder potential [10,11], where the soft repulsion is identically constant up to a certain cutoff length, and vanishes elsewhere, but other forms have been proposed as well, such as the one-parameter family considered by Jagla [12], which is again identically vanishing beyond a given cutoff, but does not feature the harsh discontinuity of the square shoulder, and can assume a variety of profiles, from a convex slide to a concave shoulder.

Despite their deceptively simple forms, these interactions give rise to a remarkable wealth of ground states featuring several lattices other than the close-packed ones, depending on the particle density and on the thickness of the soft shell compared to that of the hard core. In two dimensions this was pointed out by Jagla [12,13], and subsequently found also in the square-shoulder case, where genetic algorithms were used to find the minimum-energy configurations in both two dimensions [14,15] and three [16,17]. Indeed, even quasicrystals may occur [13,18].

Several of these nontrivial structures are characterized by the spontaneous formation of particle aggregates such as clusters, stripes, or rings [14–17]. The reason for this behavior lies in the very soft character of the shell repulsion: Because of that, the energy penalty two particles have to pay in order to come close to each other is only weakly dependent on the degree of overlap of their shells (for a square shoulder, it is actually independent of it). Particles may then find it energetically convenient to self-organize into domains made up of strongly overlapping particles separated by relatively large gaps, so that the interactions between particles belonging to different domains is very weak or absent altogether [19].

The present paper addresses the characterization of the phase consisting of two-particle clusters, i.e., dimers, with particular regard to their orientational order. It was already pointed out that the square-shoulder potential at suitably large shell-to-core ratio displays a low-density "nematic" phase, consisting of parallel dimers arranged on the sites of a slightly distorted triangular lattice [14,15]. The first issue which we address is whether the kind of arrangement reported there should be expected also for other core-softened interactions.

To this end, we consider two core-softened potentials, both of which have a smooth soft-shell part, unlike the square

---

[*] Corresponding author: francesco.mambretti@unipd.it

shoulder. Moreover, while in one of them the short-range repulsive forces are again described by a hard core, the other one features a continuous repulsion, diverging as an inverse power law at zero particle separation [20]. Our results for the ground state at density appropriate to dimer formation obtained via gradient minimization of the potential energy conform qualitatively to the picture drawn in Refs. [14,15], and highlight the central role played by the lattice distortion in stabilizing the nematic phase. In fact, removing the distortion by forcing the dimers to be located on the sites of a perfect triangular lattice would lead to a completely different kind of orientational order.

Next, we investigate whether the orientational order characteristic of the ground state is bound to survive at finite temperature. We tackle this issue by studying the behavior of particle-particle correlations obtained via accurate numerical simulations and provide evidence that this is indeed the case. In addition to the fluid-crystal transition, at which the dimers crystallize into an orientationally disordered state, there will be a second transition at a (much) lower temperature, marked by the occurrence of the nematic order of the dimers.

In detail, we discuss the pair potentials investigated in the current work and their properties in Fourier space in Sec. II. The gradient minimization method used to obtain the minimum-energy state of the system is detailed in Sec. III; the other numerical approaches used in this work, namely, Monte Carlo and parallel tempering simulations are introduced in Sec. IV. Section V presents the thermodynamic, structural, and correlation results obtained for the two models studied. The results are discussed in Sec. VI. The details of the method employed in energy minimization are described in Appendix.

II. MODEL POTENTIALS

A. Pair interactions and clustering

We consider two similar pair potentials. Each of them is based on a "soft" bounded repulsive interaction, to which we add a repulsive contribution which diverges at short range, realistically preventing a full overlap of the individual particles.

In the first instance, the soft part is a generalized exponential model of order 4 (GEM4) [21–23]

$$w_{\mathrm{GEM4}}(r) = \varepsilon \exp[-(r/R)^4] \tag{1}$$

as a function of the interparticle distance r. The parameters R and ε set respectively the range and strength of this interaction. We then add a singular hard-core repulsion of diameter δ, obtaining the hard-core plus GEM4 (HCGEM4) $\phi_{\mathrm{HCGEM4}}(r)$ potential given by

$$\phi_{\mathrm{HCGEM4}}(r) = \begin{cases} \infty & r < \delta \\ \varepsilon \exp[-(r/R)^4] & r \geqslant \delta \end{cases}. \tag{2}$$

Throughout the paper we set $\delta = 0.05\,R$, corresponding to a rather large shell to core ratio equal to 20.

The second model interaction is obtained by considering a generalized Lorentzian with exponent 6 (GL6) [24]

$$w_{\mathrm{GL6}}(r) = \frac{\varepsilon}{1 + (r/R)^6}, \tag{3}$$

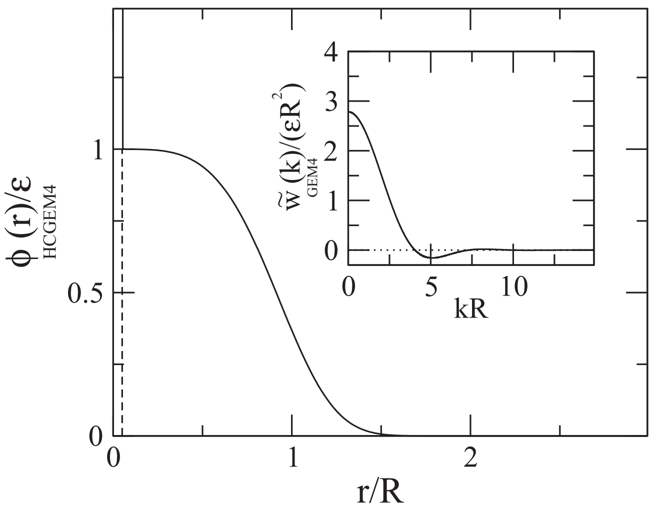

FIG. 1. Hard-core plus GEM4 potential $\phi_{\mathrm{HCGEM4}}(r)$ of Eq. (2) with hard-core diameter $\delta = 0.05R$. The inset displays the Fourier transform of the GEM4 potential $\widetilde{w}_{\mathrm{GEM4}}(k)$, exhibiting a negative minimum at $k_m \simeq 5.09618\,R^{-1}$.

with strength and range again fixed by ϵ and R. To this we add a diverging power-law repulsion of small amplitude to obtain the following smooth-core plus GL6 (SCGL6) potential:

$$\phi_{\mathrm{SCGL6}}(r) = \varepsilon\left[\frac{1}{1 + (r/R)^6} + A\left(\frac{R}{r}\right)^6\right], \tag{4}$$

where, following Ref. [20], the parameter A setting the relative strength of the diverging contribution is fixed to $A = 5 \times 10^{-5}$ throughout the paper.

Figures 1 and 2 depict the $\phi_{\mathrm{HCGEM4}}(r)$ and $\phi_{\mathrm{SCGL6}}(r)$ functions, respectively. Both the GEM4 and the GL6 potentials belong to the so-called $Q^{\pm}$ class [25], i.e., their Fourier transform changes sign and reaches a negative minimum at a nonzero wave vector k_m: in the present case, $k_m =$

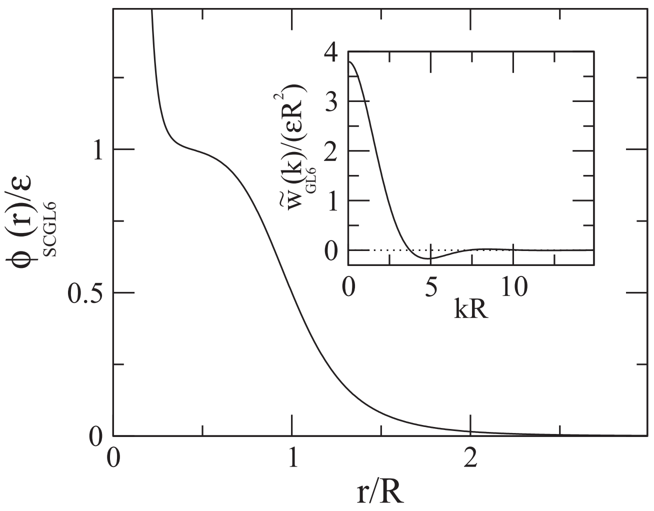

FIG. 2. Same as Fig. 1, but here for the smooth-core plus GL6 potential $\phi_{\mathrm{SCGL6}}(r)$ of Eq. (4) with smooth-core repulsion strength $A = 5 \times 10^{-5}$. The negative minimum of the Fourier transform of GL6 occurs at $k_m \simeq 4.82021\,R^{-1}$.

$5.09618\,R^{-1}$ for the GEM4 potential and $k_m = 4.82021\,R^{-1}$ for the GL6 potential, as displayed in the insets of Figs. 1 and 2.

Because of these negative minima, $Q^{\pm}$ interactions exhibit an intrinsic instability toward spontaneous density modulations, which at low temperature or high density manifest themselves as nonhomogeneous, periodic phases. The periodicity of these phases is essentially dictated by k_m: specifically, to a high degree of approximation k_m identifies with the size of a reciprocal-lattice vector [22], resulting in a nearly density-independent lattice spacing $d \propto k_m^{-1}$ in real space. As a consequence, an increase in density is brought about by having more numerous particles pile up at the same lattice site rather than by increasing the number of sites—hence clustering. Recent works have addressed the emergence of such collective phases in one-dimensional (1D) classical [26] and quantum [27,28] softly repulsive systems.

At temperatures comparable to the characteristic energy scale of the interaction, $k_\mathrm{B}T \sim \varepsilon$, the thermal average n_c of the cluster occupation number depends linearly on the average number density ρ according to

$$n_c = \rho v_0, \tag{5}$$

where $v_0 \propto d^2 \propto k_m^{-2}$ is the area of the primitive cell of the lattice of clusters. In two dimensions, the triangular lattice is expected to be the preferred structure. For a triangular lattice, one has

$$d = \frac{4\pi}{\sqrt{3}\,k_m}, \tag{6}$$

which with the above values of k_m gives $d \simeq 1.4\,R$ for the GEM4 and $d \simeq 1.5\,R$ for the GL6.

For bounded $Q^{\pm}$ interactions such as the GEM4 and the GL6, nothing prevents particles from fully overlapping with each other, so that clusters actually consist of structureless, pointlike objects in the $T \to 0$ limit. This is no longer true when a core repulsion at short distance is added, as in the HCGEM4 and the SCGL6 potentials considered here. Since cluster collapse is now prevented, clusters must necessarily grow in size as more and more particles are added into the system. Overall, such a state of affairs implies that the high-density phase behavior of these interactions is very different from that of their bounded counterparts, featuring not only clusters, but also stripes and bubbles in two dimensions [29,30], as well as more complex phases in three [31,32]. Moreover, individual clusters now exhibit an internal structure which depends on the packing behavior of the particles inside. This is especially relevant in the case of the dimer crystal we are mostly concerned with here, where all clusters consist of just two particles, and the mutual orientation of the dimers is a relevant degree of freedom of the system.

The optimal density for the occurrence of clusters with average occupation number n_c is obtained by solving Eq. (5) for ρ. For a triangular lattice, this gives

$$\rho_{n_c} = \frac{\sqrt{3}\,k_m^2}{8\pi^2} n_c. \tag{7}$$

This result is exact for the bounded, coreless, interactions, but, for small n_c and thus small ρ, it holds approximately even for the potentials considered in the present work.

At sufficiently high temperature, n_c is always determined by Eq. (5) whatever the density ρ, so that as soon as ρ deviates from ρ_{n_c}, the average occupation number will depart from the corresponding n_c. However, this no longer holds at low temperatures such that $k_\mathrm{B}T \ll \varepsilon$, and most notably at $T = 0$. In this case, the thermal motion is unable to redistribute the particles among the lattice sites, and n_c is bound to assume integer values N_c. As a consequence, densities which are far from the optimal values ρ_{N_c} must be obtained by having crystals with different N_c coexist with each other, thereby prompting a sequence or "cascade" of first-order phase transitions as ρ is increased [33,34]. For densities which do not differ much from ρ_{N_c}, the system instead finds it more convenient to adjust the lattice constant d and keep n_c fixed at N_c, like the elastic response of ordinary crystalline solids under mild compression. Therefore, at low temperature ρ does not need to coincide strictly with ρ_{N_c} for a cluster crystal with N_c particles per cluster to occur: rather, such a crystal remains stable in a certain range of densities around ρ_{N_c}. This applies in particular to the dimer case $N_c = 2$ we are interested in.

B. Dimer-dimer interaction

The total potential energy U of the system is given by

$$U = \frac{1}{2}\sum_{i\neq j} \phi(|\mathbf{x}_i - \mathbf{x}_j|), \tag{8}$$

where $\mathbf{x}_i$, $i = 1, \ldots, N$ denotes the position of the particles, N being the particle number, and ϕ is the particle-particle potential under consideration. Before studying the ground state of an assembly of interacting dimers, it is instructive to consider the case $N = 4$, i.e., the potential energy ψ of just two dimers.

Each dimer consists of two particles separated by a distance η. We indicate with $\mathbf{r}$ the vector connecting the centers of mass of the dimers and with $\boldsymbol{\eta}_\alpha$ the vector connecting the two particles forming dimer $\alpha = 1, 2$. By expanding the interparticle potential ϕ around $\mathbf{r}$ in a power series of $\boldsymbol{\eta}_\alpha$ to the second-order or quadrupole contributions, one finds for the interaction potential between the dimers

$$\begin{aligned}\psi(\mathbf{r}, \boldsymbol{\eta}_1, \boldsymbol{\eta}_2) = {}& 2\phi(\eta) + 4\phi(r) + \tfrac{1}{4}(\boldsymbol{\eta}_1 + \boldsymbol{\eta}_2)^\mathrm{T} \cdot \mathbf{H} \cdot (\boldsymbol{\eta}_1 + \boldsymbol{\eta}_2) \\ &+ \tfrac{1}{4}(\boldsymbol{\eta}_1 - \boldsymbol{\eta}_2)^\mathrm{T} \cdot \mathbf{H} \cdot (\boldsymbol{\eta}_1 - \boldsymbol{\eta}_2) + \cdots .\end{aligned} \tag{9}$$

Here the first-order dipole term vanishes, the dots denote terms higher than the quadrupole, and $\mathbf{H}$ is the Hessian matrix of $\phi(|\mathbf{r}|)$ evaluated in $\mathbf{r}$.

Since ϕ is spherically symmetric, $\mathbf{H}$ is diagonalized by choosing the axes in such a way that one of them is aligned with $\mathbf{r}$. We then obtain

$$\begin{aligned}\psi(\mathbf{r}, \boldsymbol{\eta}_1, \boldsymbol{\eta}_2) = {}& 2\phi(\eta) + 4\phi(r) + \frac{\eta^2}{2}\Big[\phi''(r)(\cos^2\gamma_1 + \cos^2\gamma_2) \\ &+ \frac{\phi'(r)}{r}(\sin^2\gamma_1 + \sin^2\gamma_2)\Big] + \cdots ,\end{aligned} \tag{10}$$

where, for $\alpha = 1, 2$, γ_α is the angle between $\mathbf{r}$ and $\boldsymbol{\eta}_\alpha$, and ϕ' and ϕ'' are the first and second derivative of ϕ, respectively. Since $\phi(r)$ is monotonically decreasing, we have clearly $\phi'(r)/r < 0$. Moreover, with $r \simeq d$, the spacing of the triangular lattice given by Eq. (6), one has $\phi''(r) > 0$ for both the HCGEM4 and the SCGL6; see Figs. 1 and 2. Under these conditions, ψ is minimum when $\gamma_1 = \gamma_2 = 90^\circ$, i.e., when the dimers are both perpendicular to $\mathbf{r}$. This effective interaction would lead to a trivial nematic orientational ground state of a hypothetical 1D chain of dimers, with all dimers aligned perpendicular to the chain line. However, in the triangular lattice at hand frustration arises, so the problem of determining the most stable configuration is nontrivial.

In the following, we will not rely on a truncated multipolar expansion such as that of Eq. (10) or its extension including higher-order terms, but will instead carry out the minimization directly on the full interaction, since we saw no clear computational advantage in expanded forms.

III. DETERMINATION OF THE GROUND STATE

To investigate the $T = 0$ equilibrium configuration of the model, we need to determine the most stable arrangement of an assembly of interacting dimers. Since there is no kinetic contribution to the energy, this amounts to finding the configuration which minimizes the potential energy U at fixed ρ. To this end, we adopt different minimization methods for the HCGEM4 and SCGL6 potentials, as described in the following.

A. The HCGEM4 potential

For the HCGEM4 potential, the hard-core repulsion has no effect on cluster formation until the interparticle distance is exactly equal to the hard-core diameter δ, at which point further approach between the particles is strictly forbidden. Therefore, the dimer size η must coincide with δ for all dimers. Leaving out the possibility of helical or other incommensurately ordered phases, we will henceforth assume that the system consists of a periodic arrangement of such dimers. This is obtained by translating a supercell of area v containing n dimers along the vectors of a two-dimensional (2D) lattice. The resulting lattice is endowed with a $2n$-particle basis. While $n = 1$ is sufficient to describe a simple nematic crystal, one has to allow for a suitably large n in order to account for the possibility of more complex forms of orientational order. Denoting the position of a generic particle of the system by $\mathbf{x}_i$, we have

$$\mathbf{x}_i = \mathbf{R} + \mathbf{r}_{\alpha\sigma}, \tag{11}$$

where the vector $\mathbf{R}$ identifies the position of the lattice site, and $\mathbf{r}_{\alpha\sigma}$ is the basis vector which identifies the position of the particle inside the supercell according to

$$\mathbf{r}_{\alpha\sigma} = \mathbf{u}_\alpha + \sigma\frac{\boldsymbol{\eta}_\alpha}{2}. \tag{12}$$

Here $\mathbf{u}_\alpha$ and $\boldsymbol{\eta}_\alpha$, $\alpha = 1, \dots, n$ are the vectors which determine respectively the position of the center of mass and the orientation of the αth dimer, and $\sigma = \pm 1$ is the index identifying the two particles in a dimer. We denote by $\mathbf{A}$ the (nondegenerate) 2×2 matrix formed by the two primitive vectors of the 2D lattice. In these terms, Eq. (12) can be rewritten as

$$\mathbf{r}_{\alpha\sigma} = \mathbf{A}\cdot \mathbf{s}_\alpha + \sigma\frac{\eta}{2}\begin{pmatrix}\cos\vartheta_\alpha \\ \sin\vartheta_\alpha\end{pmatrix}, \tag{13}$$

where $\mathbf{s}_\alpha = \mathbf{A}^{-1}\mathbf{u}_\alpha$ is a point of the square $[\,0, 1) \otimes [\,0, 1)$ and ϑ_α is the angle between $\boldsymbol{\eta}_\alpha$ and the x-axis, with $0 \leqslant \vartheta_\alpha < \pi$.

By arranging the particles into dimers of length δ the effect of the hard-core interaction between particles belonging to the same dimer is taken into account from the outset. This is not true in general when the particles belong to different dimers. However, as observed in Sec. II A, δ is much smaller than the lattice constant d intrinsic to the GEM4 potential. When searching for the optimal configuration, the instances in which the hard-core interaction between particles belonging to different dimers would come into play can then be safely ruled out, as can be also verified *a posteriori*. As a consequence, in the calculation of the dimer-dimer contribution to U one can consider only the soft-core part of the interaction $w_{\mathrm{GEM4}}(r)$. The total potential energy is given by Eq. (8), where the interparticle potential ϕ can be replaced by $w \equiv w_{\mathrm{GEM4}}$.

We introduce the microscopic density function $\hat{\rho}(\mathbf{x})$ defined by

$$\hat{\rho}(\mathbf{x}) = \sum_{\mathbf{R},\alpha,\sigma} \delta^{(2)}(\mathbf{x} - \mathbf{R} - \mathbf{r}_{\alpha\sigma}), \tag{14}$$

where $\delta^{(2)}(\mathbf{x})$ is the Dirac delta distribution in two dimensions. For a system consisting of N particles, the potential energy U can be expressed in terms of $\hat{\rho}$ as

$$U = \frac{1}{2}\int d^2\mathbf{x}\, d^2\mathbf{x}'\, \hat{\rho}(\mathbf{x})\hat{\rho}(\mathbf{x}')w(|\mathbf{x} - \mathbf{x}'|) - \frac{1}{2}Nw(0). \tag{15}$$

By taking the periodicity of $\hat{\rho}(\mathbf{x})$ into account, the integral over $\mathbf{x}$ and $\mathbf{x}'$ is conveniently expressed in Fourier space. This gives an energy per particle

$$E \equiv \frac{U}{N} = \frac{1}{4nv}\sum_{\mathbf{G}} \widetilde{w}(G)\Big|\sum_{\alpha,\sigma} e^{-i\mathbf{G}\cdot\mathbf{r}_{\alpha\sigma}}\Big|^2 - \frac{1}{2}w(0), \tag{16}$$

where $\widetilde{w}(G)$ is the 2D Fourier transform of $w(r)$, G is the modulus of the reciprocal vector $\mathbf{G}$, and the $\mathbf{G}$ sum runs over the reciprocal lattice $\mathbf{G} = \mathbf{B}\cdot\mathbf{m}$, $\mathbf{m}$ being a vector with integer components, and $\mathbf{B}$ the 2×2 matrix related to the matrix $\mathbf{A}$ of the direct lattice by $\mathbf{B} = 2\pi(\mathbf{A}^{\mathrm{T}})^{-1}$. The scalar product $\mathbf{G}\cdot\mathbf{r}_{\alpha\sigma}$ in Eq. (16) can then be expressed as

$$\mathbf{G}\cdot\mathbf{r}_{\alpha\sigma} = 2\pi\,\mathbf{m}\cdot\mathbf{s}_\alpha + \sigma\frac{\eta}{2}\,\mathbf{m}\cdot\mathbf{B}^{\mathrm{T}}\cdot\begin{pmatrix}\cos\vartheta_\alpha \\ \sin\vartheta_\alpha\end{pmatrix}. \tag{17}$$

Without loss of generality, one of the primitive vectors of the reciprocal lattice can be aligned along the y-axis, thereby implying that one of the primitive vectors of the direct lattice is aligned along the x-axis. Moreover, there is a constraint on $\mathbf{B}$ due to the fact that the cell area $v = 4\pi^2/\det\mathbf{B}$ is also fixed by the relation $v = 2n/\rho$. Hence, for a given average density ρ, we are left with just two independent elements of $\mathbf{B}$, say b_1 and b_2:

$$\mathbf{B} = \begin{pmatrix} b_1 & 0 \\ b_2 & \dfrac{p}{b_1}\end{pmatrix}, \tag{18}$$

where we have set $p = 4\pi^2/v$.

In the most general situation (see Sec. V), we minimize the energy per particle (16) with respect to the n vectors $\mathbf{s}_\alpha$, the n angles ϑ_α, and the matrix elements b_1, b_2, i.e., with respect to the positions of the dimer centers inside the cell, the dimer orientations, and the cell axes. We carry out the minimization by an iterative algorithm similar to that adopted in Refs. [31,35] for the mean-field free-energy functional in order to describe the mesophases of fluids [31] and fluid mixtures [35]. The method is a refinement of the basic steepest descent [36], whereby each variable is updated recursively by moving "downhill" in the direction opposite to that of the gradient of the function E to be minimized according to

$$\vartheta_\alpha^{\,l+1} = \vartheta_\alpha^{\,l} - \lambda \left.\frac{\partial E}{\partial \theta_\alpha}\right|_l \tag{19}$$

and the corresponding expressions for $\mathbf{s}_\alpha$, b_1, b_2, until convergence is obtained to a prescribed accuracy. In the above equation, the index l refers to the iteration stage, and the parameter λ gives the size of the downhill step. Compared to the basic version of Eq. (19), the modifications introduced to increase the convergence speed consist in determining the direction of descent by conjugate gradients with preconditioning rather than by the gradient alone, and in changing the stepsize λ adaptively at each iteration instead of keeping it fixed. The details of the method are provided in Appendix.

As an example of starting condition for the minimization, we initialize the supercell as a rhombus with sides $\ell\mathbf{e}_1$ and $\ell\mathbf{e}_2$, where ℓ is a positive integer and $\mathbf{e}_1$, $\mathbf{e}_2$ are the primitive vectors of the triangular lattice given by

$$\mathbf{e}_1 = d\,\mathbf{e}_x, \tag{20}$$

$$\mathbf{e}_2 = \frac{d}{2}\,\mathbf{e}_x + \frac{\sqrt{3}}{2}d\,\mathbf{e}_y, \tag{21}$$

where $\mathbf{e}_x$ and $\mathbf{e}_y$ are the coordinate unit vectors. The lattice spacing

$$d = \frac{2}{(\sqrt{3}\rho)^{1/2}} \tag{22}$$

is determined by setting $n_c = 2$ in Eq. (5). Clearly, if ρ coincides exactly with the optimal value for dimer formation given by Eq. (7) for $n_c = 2$, then the lattice spacing coincides with that of Eq. (6). However, as discussed in Sec. II A, a dimer crystal is expected in a whole range of densities close to that value. Since the supercell thus obtained contains ℓ^2 primitive cells, each of which contains one dimer, we have $n = \ell^2$ dimers per supercell. We initialize the n positions $\mathbf{s}_\alpha$ either by putting the dimers at random positions inside the cell, or by arranging them regularly on the sites of the lattice generated by $\mathbf{e}_1$ and $\mathbf{e}_2$. In the former case, the components $s_{\alpha1}$, $s_{\alpha2}$ of $\mathbf{s}_\alpha$ are random numbers in the interval [0,1), whereas in the latter case they are given by

$$s_{\alpha1} = \frac{j_1 - 1}{\ell}, \qquad s_{\alpha2} = \frac{j_2 - 1}{\ell}, \qquad j_1, j_2 = 1, \ldots, \ell, \tag{23}$$

with the index $\alpha = j_1 + (j_2 - 1)\ell$. For the initial orientation of the dimers specified by the angles ϑ_α, we tested both random values, or some nematic state corresponding to the same value of ϑ_α for all dimers, or by having ϑ_α increase by a fixed amount when moving from one dimer to the adjacent one. We performed minimizations on cells containing up to $n = 10^2$ dimers, sufficient to allow us to detect rather complex forms of orientational order, if present.

B. The SCGL6 potential

Unlike the HCGEM4, for the SCGL6 potential the smooth-core character of the repulsion at short range implies that the dimer size η is not determined from the beginning. Although we expect that its equilibrium value will be near the inflection point of ϕ_{SCGL6} corresponding to the minimum of the repulsive force, η should nevertheless be considered as a degree of freedom of the system which, in principle, is different for each dimer. It would again be possible to split the interaction into a regular and a singular contribution, but it is not possible to take the latter into account *a priori* by just putting the dimer particles at some fixed distance η from each other: Hence, the minimization must involve the interaction ϕ_{SCGL6} as a whole, including its singular part whose Fourier transform is not defined.

This makes the procedure described in Sec. III A unsuited for the SCGL6 potential. In principle, the singularity could be removed by introducing some small cutoff distance $r_c \ll R$, such that the value of ϕ_{SCGL6} at r_c is much larger than that at the inflection point, and setting the potential identically equal to $\phi_{\mathrm{SCGL6}}(r_c)$ for $r < r_c$. However, in the interaction this would introduce a further characteristic length r_c besides the natural length scale R, resulting in a painfully slowly decaying tail of its Fourier transform. The latter should be sampled at intervals much smaller than $\sim 2\pi/R$, and over a domain much larger than $\sim 2\pi/r_c$. Such a daunting scenario is largely sufficient to make this strategy unviable, because of the exceedingly large number of reciprocal lattice vectors which should be included in the $\mathbf{G}$-summation of Eq. (16).

Accordingly, we perform the minimization of the potential energy per particle E in real space, using the same refined steepest-descent algorithm adopted for the HCGEM4 interaction. Moreover, since the dimer size is not known from the beginning, we do *not* start from dimerized configurations, and we minimize E with respect to the positions of all the $2n$ particles inside the supercell.

We replace Eq. (11) by $\mathbf{x}_i = \mathbf{R} + \mathbf{r}_\alpha$, with $\mathbf{R} = \mathbf{A}\cdot\mathbf{m}$ and $\mathbf{r}_\alpha = \mathbf{A}\cdot\mathbf{s}_\alpha$, $\mathbf{m}$ being a vector with integer components and $\mathbf{s}_\alpha \in [0, 1) \otimes [0, 1)$ as in Sec. III A. Here the vector $\mathbf{r}_\alpha$, $\alpha = 1, \ldots, 2n$, identifies the position of the particle itself inside the supercell instead of the center of mass of the dimer, and the matrix $\mathbf{A}$ is the same of Eq. (13). The energy per particle is then

$$E = \frac{1}{4n}\sum_{\alpha\neq\alpha'}\phi(\mathbf{r}_\alpha - \mathbf{r}_{\alpha'}) + \frac{1}{4n}\sum_{\mathbf{R}\neq 0}\sum_{\alpha,\alpha'}\phi(\mathbf{R} + \mathbf{r}_\alpha - \mathbf{r}_{\alpha'}), \tag{24}$$

where we have separated the contribution of particles in the same cell from those in neighboring ones.

We write matrix $\mathbf{A}$ as

$$\mathbf{A} = \begin{pmatrix} a_1 & a_2 \\ 0 & v/a_1 \end{pmatrix}, \tag{25}$$

where the constraint $v = 2n/\rho$ on the supercell area v leaves only two independent elements as in Eq. (18). The steepest-descent algorithm is then performed on Eq. (24) by iteratively updating $\mathbf{s}_\alpha$, a_1, a_2 until convergence is reached.

For the SCGL6 potential, we refer to the results of Ref. [20]. In fact, that paper was mainly concerned with the out-of-equilibrium dynamics of the SCGL6 model under external forces, but some investigation of its low-energy properties was nevertheless carried out. To make contact with those results, we adopt the same conditions considered there. Specifically, the density is fixed at the value $\rho_2 = 1.02640\,R^{-2}$ obtained from Eq. (5) for a triangular lattice such that the size of its primitive cell $v_0 = \sqrt{3}\,d^2/2$ is determined by setting the lattice constant d exactly at $d = 1.5\,R$, close to $d = 1.50516\,R$ as per Eq. (6) (which would yield the similar value $\rho_2' = 1.01937\,R^{-2}$).

For a given accuracy, the power-law decay of the SCGL6 potential requires a larger cutoff distance than for the exponentially decaying HCGEM4. Following Ref. [20] we truncate the potential at the distance $r_c = 5R$, applying the standard linear shift that makes the truncated potential continuous and differentiable at r_c. The $\mathbf{R}$-summation in Eq. (24) includes sufficiently many supercell translations to reach r_c in all directions.

We carry out the minimizations for up to $2n = 10$ particles per supercell. By randomly initializing the particle positions inside the box, we cannot rule out the occasional occurrence of configurations which do not correspond to a pure-dimer phase but feature, for instance, also monomers and trimers. Such configurations are systematically higher in energy than the fully dimerized ones and are therefore disregarded.

IV. SIMULATIONS

In order to complement the minimization techniques described above, and to extract some physical insights into the low-temperature behavior of the HCGEM4 model, we resort to stochastic simulation methods. On one hand, this method allows us to further characterize the overall ground state of the HCGEM4 potential, and, on the other hand, it provides finite-temperature properties, which remain outside the scope of the gradient minimization technique. In particular, we exploit the parallel tempering (PT) approach [37] to locate the optimal dimer configuration at extremely low temperature. We then give the latter as input to a code that performs a Metropolis [38] Monte Carlo (MC) simulation in the canonical ensemble. These codes are available on GitHub [39] with the related documentation. The PT procedure concurrently runs many MC simulations at different fixed temperatures T_i, with periodic attempts to exchange configurations across simulations at adjacent temperatures. Specifically, following the work by Kofke [40], we run n_{PT} concurrent simulations, with temperatures set as

$$T_i = \left(\frac{T_{\max}}{T_{\min}}\right)^{1/n_{\mathrm{PT}}} T_{i-1}. \qquad (26)$$

For studying the low-temperature physics of this model, we take $T_{\max} = 2 \times 10^{-5}\,\varepsilon/k_{\mathrm{B}}$ and $T_{\min} = 1 \times 10^{-9}\,\varepsilon/k_{\mathrm{B}}$ for the maximum and minimum temperatures explored, and $n_{\mathrm{PT}} = 272$. In this way, the simulation with the lowest temperature investigated should reach the minimum-energy equilibrium configuration in a long but finite number of steps.

To better characterize the stability of the obtained ground-state configuration, we run a subsequent MC simulation at temperature $T = 100 \times T_{\min} = 10^{-7}\epsilon/k_{\mathrm{B}}$. This value is a trade-off between the target of the vanishing temperature limit and the need for a significant acceptance of the MC moves.

The MC and PT codes are inherently parallel and naturally leverage a simple MPI-parallelized approach on high-performance multiprocessor computer systems. In both approaches, we employ single-particle moves with respective amplitudes tuned to obtain satisfactory acceptance ratios and cluster moves (rotations, rigid translations, and modifications of intracluster particle distances) as well. The results presented in the following are obtained by placing the core-softened particles in a rectangular box which contains $M \times M$ dimer units, corresponding to $N = 2M^2$ particles, initially located in pairs at the sites of a triangular lattice. The aspect ratio of the two box sides is chosen in order to accommodate the triangular lattice or is allowed to vary, keeping the density fixed, to allow the lattice structure to distort. Further details about the simulation setup and the original codes with input files are provided as an online GitHub repository [39].

In the simulations, we replace the hard core of the HCGEM4 potential with a finite-amplitude step by defining the interaction as $\varepsilon \exp[-(r/R)^4] + K$ for $r < \delta$, with $K = 5\varepsilon$, with the advantage of allowing us to Fourier-transform this regularized HCGEM4 potential. At the investigated temperatures this regularization does not affect the behavior of the system, since the statistical weight of the configurations with mutually overlapping particles can safely be taken as zero.

We execute all simulations at the density $\rho_2 = 1.13971\,R^{-2}$ obtained from Eq. (7) with $n_c = 2$ and $k_m = 5.09679\,R^{-1}$. The latter was obtained by including the step function in the evaluation of the Fourier transform of the interaction, whereas the value $k_m = 5.09618\,R^{-1}$ of the "pure" GEM4 potential reported in Sec. II A would give $\rho_2' = 1.13944\,R^{-2}$. Clearly, ρ_2 and ρ_2' are very close, and, according to the discussion of Sec. II A, there is no reason to discard either of them, as they both lie in the density interval where dimers prevail in the ground state. Since ρ_2 is the value used in the simulations, gradient minimizations are carried out at this same density for direct comparison.

V. RESULTS

A. The HCGEM4 model

As a preliminary investigation, we perform both MC simulations and gradient minimizations by arranging the centers of mass of the dimers at fixed positions, given by the sites of the triangular lattice with spacing $d = 1.42348\,R$ obtained from substituting the appropriate value of k_m in Eq. (6), or equivalently of ρ_2 in Eq. (22). Hence, only the orientational degrees of freedom ϑ_α are taken into account. In the minimization, the supercell parameters b_i are then kept fixed at the values $b_1 = 2\pi/d$, $b_2 = -2\pi/(\sqrt{3}d)$, and the positional parameters $\mathbf{s}_\alpha$ are kept fixed at their initial values, Eq. (23).

At the end of the minimization, the configurations thus obtained consist of alternating rows of parallel dimers in a herringbone-like arrangement, such that the dimer orientation is the same every other row, whereas dimers belonging to adjacent rows have different orientations. Specifically, if along a certain row the dimers are oriented at an angle γ with respect to the row direction, the angle will be $-\gamma$ for the adjacent rows. We are then in the presence of *antinematic* order.

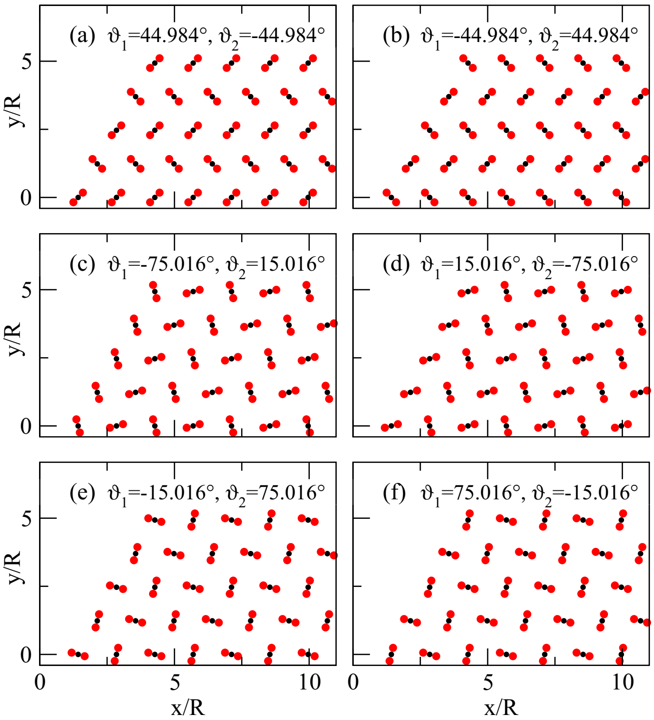

FIG. 3. The six degenerate antinematic states of lowest energy at $T = 0$ for a dimer crystal on a triangular lattice (black dots). The interaction is HCGEM4, and the density is $\rho = 1.13971\,R^{-2}$. The dimer length is magnified by a factor 10 relative to the actual value $\delta = 0.05\,R$ for ease of readability. The angles ϑ_1, ϑ_2 between the directions of the dimers and the horizontal axis are specified in each panel.

There are six symmetry-equivalent degenerate antinematic states, as displayed in Fig. 3. In panels (a) and (b), the rows of parallel dimers are aligned along the x-axis, i.e., with the primitive vector $\mathbf{e}_1$; see Eq. (20). The equivalent minima of panels (c) and (e) could be obtained from that of panel (a) by a rigid rotation of 60° and −60°, respectively, so that the rows of parallel dimers are directed along $\mathbf{e}_2$ in panel (c) and along $\mathbf{e}_2 - \mathbf{e}_1$ in panel (e). The same considerations apply for the states of panels (d) and (f) starting from that of panel (b). Moreover, panels (b), (d), and (f) can be obtained from panels (a), (c), and (e) by swapping neighboring rows of parallel dimers.

MC simulations can determine the dimer orientations with an accuracy of $\sim 1^\circ$. Within this accuracy, the angle γ between a row of parallel dimers and the dimer direction is indistinguishable from $\gamma = \pm 45^\circ$. This would imply that dimers belonging to adjacent rows are perpendicular to each other, and form with the x-axis the angles ϑ_1, ϑ_2 given by $(45^\circ, -45^\circ)$, $(-45^\circ, 45^\circ)$, $(-75^\circ, 15^\circ)$, $(15^\circ, -75^\circ)$, $(-15^\circ, 75^\circ)$, $(75^\circ, -15^\circ)$ for the configurations displayed in Figs. 3(a)–3(f). The gradient minimization of the potential energy brings out tiny differences from the above values. Specifically, we find $\gamma = \pm 44.984^\circ$, so that dimers in adjacent rows are not strictly perpendicular, but form an angle $2\gamma = 89.968^\circ$. Similarly, the angles ϑ_1, ϑ_2 between the dimer orientations and the x-axis do not coincide exactly with those listed above, but assume the values reported in each panel of Fig. 3. The difference between the potential energy of the configurations featuring perfectly perpendicular dimers and those obtained by the gradient minimization amounts to a tiny $\Delta E = 1.65 \times 10^{-12}\,\varepsilon$. We believe these tiny deviations to be genuine, since the same values of ϑ_1, ϑ_2 were obtained from different initial configurations in multiple minimization runs. Moreover, we verified that the deviations from 45° increase on increasing the dimer length δ. This leads us to surmise that configurations corresponding to rigorously perpendicular dimers would be obtained only in a hypothetical limit $\delta \to 0$ of purely quadrupolar dimer-dimer interactions.

The potential energy per particle at $T = 0$ predicted by the gradient minimization agrees with that obtained from the numerical simulations at $T_{min} = 1 \times 10^{-9}\,\varepsilon/k_{\mathrm{B}}$ within seven significant digits and amounts to $E = 0.60195430\,\varepsilon$. Observe that approximately 83% of the energy is accounted for by the trivial intracluster contribution E_{intra} due to the interaction between particles within the same dimer, $E_{\mathrm{intra}} = w_{\mathrm{GEM4}}(\delta)/2 \simeq 0.5\,\varepsilon$. Moreover, its value is close to that obtained by arranging on the same triangular lattice an assembly of pointlike dimers interacting solely via the soft-core potential w_{GEM4} in the absence of hard-core repulsion, $E_{\mathrm{soft}} = 0.59884959\,\varepsilon$. Hence, in purely quantitative terms the effect of the finite dimer size and of orientational order on the overall energy balance is comparatively modest.

Despite the good agreement between gradient minimizations and MC simulations in the description of the perfect-lattice antinematic phase, simulations also provide strong evidence that this phase does *not* represent the actual ground state of the system. Indeed, releasing the positions of the dimers leads to a lowering of E and to different particle arrangements, whereby dimers are placed at positions slightly deviating from those of a triangular lattice.

Figure 4 shows two examples of such arrangements: Figs. 4(a) and 4(b) represent snapshots of the relaxed configuration of two MC simulations with $N = 968$ and 1800 particles in the supercell, respectively. Evidently, these configurations do not exhibit antinematic order but rather large domains of mostly local nematic character with four vortex-like topological defects (marked by red and blue crosses) located at the boundary between different domains. Defects carry a topological charge or winding number W,

$$W = \frac{1}{2\pi} \sum_{i(\gamma)} (\theta_{i+1} - \theta_i) \to \frac{1}{2\pi} \oint_{\gamma} d\theta, \tag{27}$$

where γ stands for any closed path surrounding one vortex, the angles θ_i are the angles of the dimers along the path, and these angles can be promoted to a smooth function θ in the continuum limit. For the configurations in hand, we consistently find $W = \pm 1/2$.

As the simulation box grows larger, the distance between defects increases, thus enlarging the size of the partially ordered nematiclike regions, with no sign of approaching any asymptotic limit—at least up to the largest systems accessible to MC simulations. Meanwhile, for increasing box size the energy per particle keeps decreasing steadily. This suggests that, rather than being a feature intrinsic of the ground state, defects are extrinsic effects due to finite size: they are bound to become infinitely dilute in the thermodynamic limit.

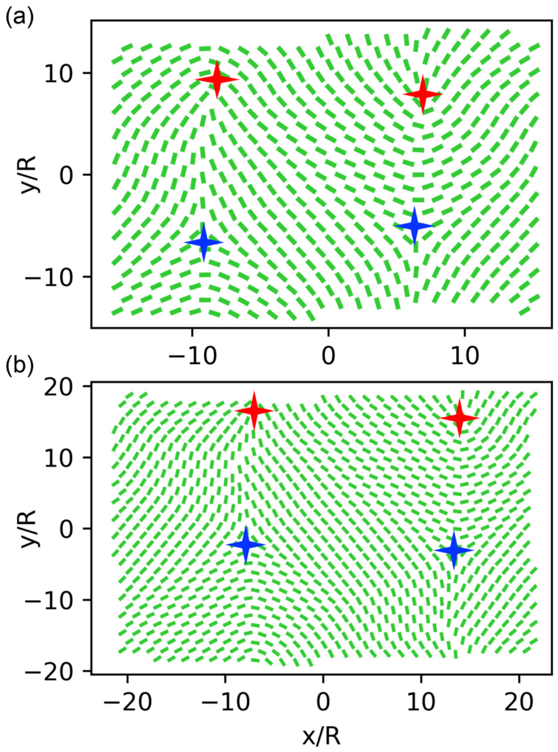

FIG. 4. Examples of sampled MC configurations, for the relaxed states of dimers (represented as small green dashes) of particles interacting via a HCGEM4 potential at $T = 10^{-7}\,\varepsilon/k_B$. In these simulations, the rectangular box aspect ratio is kept fixed to the value compatible with the triangular lattice. (a) A configuration of 968 particles. (b) A configuration of 1800 particles. Red and blue crosses mark the positions of the topological defects with charge $W = \pm 1/2$ induced by the periodic boundary conditions incompatible with the actual nematic ground state.

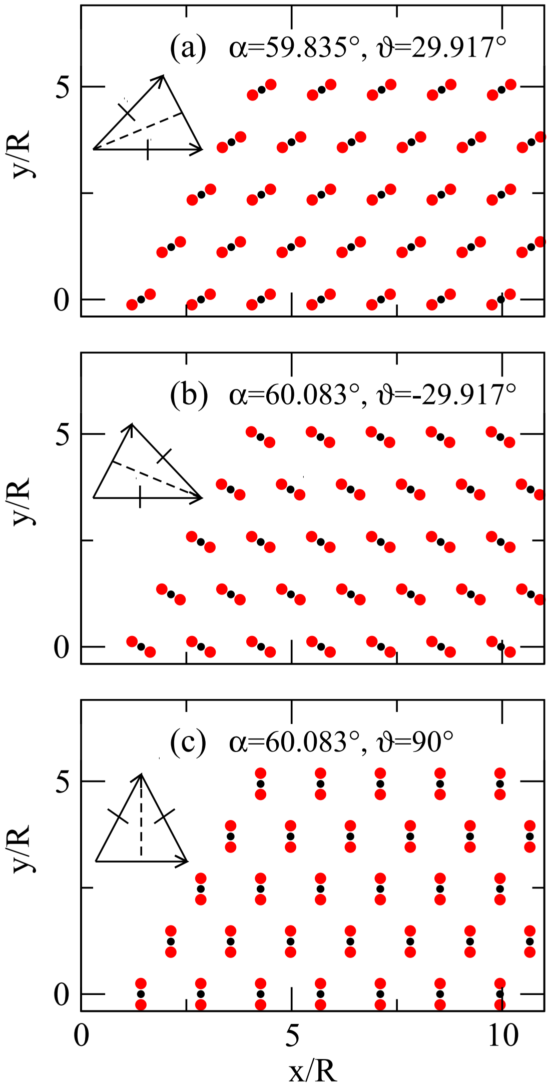

FIG. 5. Three orientations of the nematic ground state for a dimer crystal at $\rho = 1.13971\,R^{-2}$. The dimer size is magnified by a factor 10 as in Fig. 3. In each panel, α is the angle between the primitive vectors $\mathbf{e}_1$, $\mathbf{e}_2$, and ϑ is the angle between the direction of the dimers and the horizontal axis. The insets give a qualitative representation of the lattice vectors (not to scale). The arrows represent the primitive vectors $\mathbf{e}_1$ and $\mathbf{e}_2$. The ticks mark the sides of equal length of the isosceles triangles. The dashed symmetry axis marks the direction of the nematic alignment.

Prompted by the evidence above, we proceed to execute gradient minimizations of the potential energy by releasing the constraint on the unit cell and the dimer positions, according to the procedure described in Sec. III. As above, the direction of the x-axis is identified by the lattice vector $\mathbf{e}_1$.

We find that the lattice undergoes a small distortion from the triangular lattice: specifically, the angle between the vectors $\mathbf{e}_1$, $\mathbf{e}_2$ of the primitive cell decreases from 60° to $\alpha_0 = 59.835^\circ$, and their length increases to $|\mathbf{e}_1| = |\mathbf{e}_2| = d' = d\,(2\sin\alpha_0/\sqrt{3})^{-1/2} = 1.42467\,R$ from the spacing $d = 1.42348\,R$ of the triangular lattice with equal density. With this angular distortion, $\mathbf{e}_1$ and $\mathbf{e}_2$ generate a centered rectangular lattice. The triangle formed by $\mathbf{e}_1$, $\mathbf{e}_2$, and $\mathbf{e}_1 - \mathbf{e}_2$ has then two sides of length d' and one side of length $|\mathbf{e}_1 - \mathbf{e}_2| = d'' = d\,[\sqrt{3}\tan(\alpha_0/2)]^{1/2} = 1.42111R$. A minimal hexagon formed by the six sites surrounding any given lattice site has four sides of length d' and two sides of length d''.

This small structural distortion has, however, a dramatic effect on the dimer arrangement, which changes from antinematic to nematic. The dimer direction forms an angle $\vartheta = \alpha_0/2 = 29.917^\circ$ with the x-axis, so that it lies midway between $\mathbf{e}_1$ and $\mathbf{e}_2$, as illustrated in Fig. 5(a).

As illustrated in Figs. 5(b) and 5(c), symmetry generates two equivalent degenerate nematic configurations, which are obtained from that just described by rotating the lattice either clockwise by α_0 or counterclockwise by $90^\circ - \alpha_0/2 = 60.083^\circ$. The one represented in Fig. 5(b) has $|\mathbf{e}_1| = d'$, $|\mathbf{e}_2| = d''$. The angle between $\mathbf{e}_1$ and $\mathbf{e}_2$ is $90^\circ - \alpha_0/2$, and the nematic angle ϑ is $-\alpha_0/2$. The configuration of Fig. 5(c) has $|\mathbf{e}_1| = d''$, $|\mathbf{e}_2| = d'$. The angle between the two lattice vectors is again $90^\circ - \alpha_0/2$, and the nematic angle is $\vartheta = 90^\circ$.

We remark that, unlike what would happen for the triangular lattice, the distorted lattice is not mapped into itself by the above rotations. Hence, these degenerate configurations differ from one another not only in the direction of the nematic axis, but also in the positions of the lattice points, although the deformation relative to the triangular lattice is too small

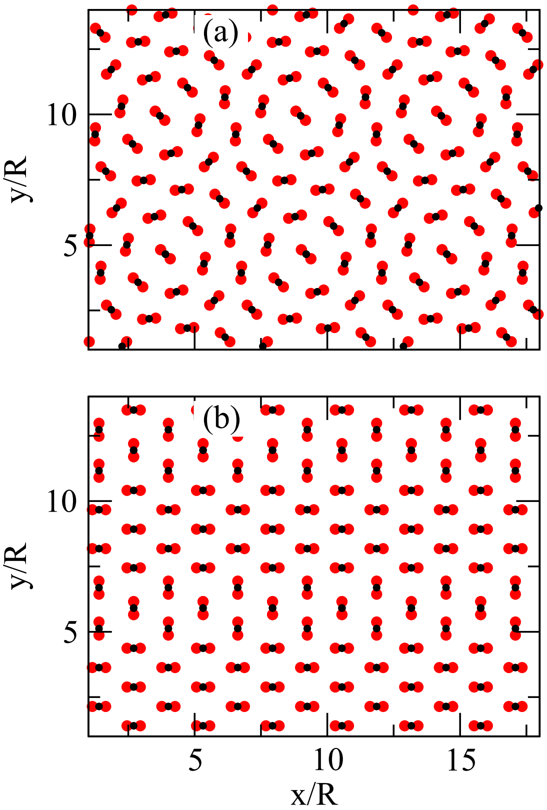

FIG. 6. Two examples of metastable configurations representing local minima of the total energy U of a dimer crystal at $\rho = 1.13971\,R^{-2}$. In both cases, the dimer length is magnified by a factor 10 as in Fig. 3, and the unit cell is replicated several times in order to illustrate the periodicity. The energy per particle amounts to (a) $E = 0.68577624\,\varepsilon$ and (b) $E = 0.75980667\,\varepsilon$, both well above the nematic ground state.

to make this feature detectable on the scale of the figure. A schematic representation of the primitive vectors of each lattice is displayed as an inset in each panel.

The potential energy per particle of this nematic state amounts to $E = 0.60194784\,\varepsilon$. E is of course lower (by approximately $6.5 \times 10^{-6}\,\varepsilon$) than that of the antinematic state described above. Once the supercell vectors are left free to adjust, releasing also the constraint on the dimer positions inside the cell does not yield any substantial change in the lowest-energy configuration, compared to those obtained by nailing the dimer centers of mass to the centered-rectangular lattice sites according to Eq. (23). Specifically, the periodic nematic state of Fig. 5 can be rigorously mapped into each one of the unconstrained minima by combining a translation and a rotation.

Other, more complex dimer arrangements do occur, such as those displayed in Fig. 6. However, their energies are systematically higher than that of the nematic configuration characterized above, which then represents the *bona fide* ground state of the system.

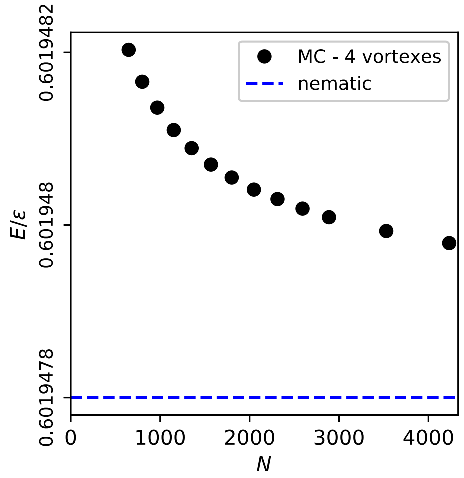

FIG. 7. Simulated potential energy per particle E in ε units (black dots) at $T = 10^{-9}\,\varepsilon/k_\mathrm{B}$ as a function of the number of particles N, in the presence of four vortices generated by the rectangular box aspect ratio kept fixed to the value compatible with the triangular lattice, as in Fig. 4. Error bars are smaller than the symbol size. The energy of the nematic ground state (Fig. 5) obtained by gradient minimization is shown as a blue dashed line.

The energy of the nematic configuration of Fig. 5 is also lower than that of the four-vortex configurations of the type of Fig. 4 which, for the largest simulated size, lies at $E = 0.60194795(5)\,\varepsilon$. Figure 7 reports a comparison between the optimum energy per particle obtained from gradient minimization and the values obtained from MC simulations at $T = 10^{-7}\,\varepsilon/k_\mathrm{B}$ as a function of the particle numbers N (equivalent to the supercell size). Up to the largest simulated supercell ($N = 4232$ particles, requiring a considerable computational effort), it is evident that the energy per particle extracted from MC simulations is still decreasing upon increasing N. The apparent asymptotic trend of the black dots suggests that the nematic energy found by the minimization method could be reached in simulations only by releasing a constraint imposed by the periodic boundary conditions in a fixed supercell. To verify this hypothesis, we run an additional set of PT simulations featuring the possibility to adjust the aspect ratio of the box. Once the fixed-supercell constraint is released, PT simulations reach one of the three nematic ground states of Fig. 5, with the same potential energy per particle found via gradient minimization, within statistical error.

Aiming to characterize the thermal stability and equilibrium properties of the nematic state, we pick the final PT configuration at $T = 10^{-9}\,\varepsilon/k_B$ and adopt it as starting configuration for the MC code at several temperatures. The MC simulations carried out at $T = 10^{-7}\varepsilon/k_B$ yield a potential energy per particle equal to $0.6019478181(1)\,\varepsilon$, which again agrees with the ground-state energy obtained by means of gradient minimization within seven significant digits. Moreover, topological defects such as those displayed in Fig. 4 no longer occur, and visual inspection of the simulation snapshots at equilibrium is now fully consistent with the nematic ground state.

As a further characterization of nematic ordering, consider the structure factor

$$S(\mathbf{q}) = \frac{1}{N}\left\langle \sum_{j,l} e^{i\mathbf{q}\cdot(\mathbf{x}_j-\mathbf{x}_l)} \right\rangle, \tag{28}$$

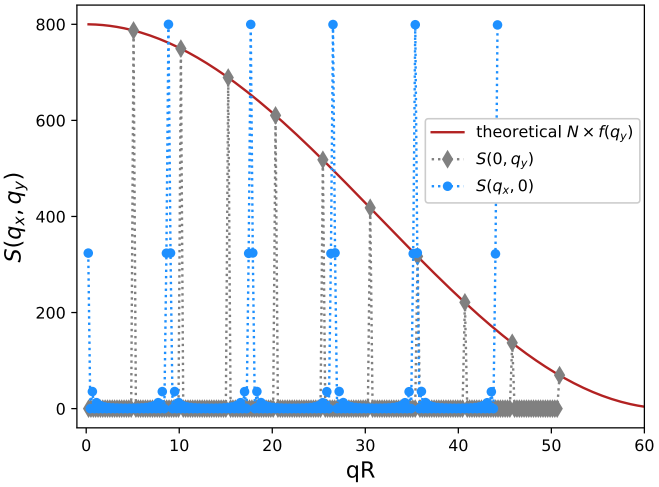

FIG. 8. $S(q_x, 0)$ (blue circles) and $S(0, q_y)$ (gray diamonds), obtained by $T = 10^{-7}\varepsilon/k_{\rm B}$ MC simulations for $N = 800$ particles in the nematic state sketched in Fig. 5(c). Red line: $N \times f(q_y)$, Eq. (32) ($T = 0$ theoretical prediction).

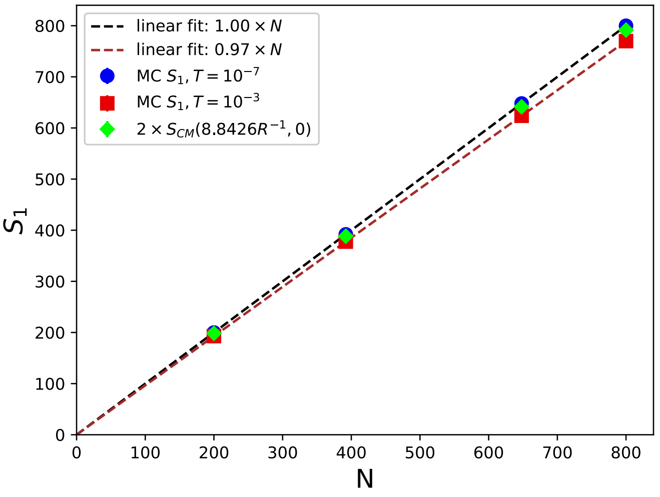

FIG. 9. Scaling of the first Bragg peak intensity S_1 as a function of N, where the data points are taken from simulations of $S(q_x, 0)$ carried out in supercells compatible with the centered-rectangular lattice, and $\alpha_0 = 59.835^\circ$ at temperatures $T = 10^{-7}\,\varepsilon/k_{\rm B}$ (blue circles) and $T = 10^{-3}\,\varepsilon/k_{\rm B}$ (red squares). The dashed lines are linear fits of the simulated data. Green diamonds signify twice the intensity of the corresponding Bragg peak $S_{\rm CM}(8.8426\,R^{-1}, 0)$ in the structure factor of the dimer centers of mass at $T = 10^{-3}\,\varepsilon/k_{\rm B}$, which is only sensitive to phonon excitations, not to thermal fluctuations in the dimers orientation.

where angular brackets denote thermal average. Analogously, we define

$$S_{\rm CM}(\boldsymbol{q}) = \frac{1}{n}\left\langle \sum_{\alpha,\alpha'} e^{i\mathbf{q}\cdot(\mathbf{u}_\alpha - \mathbf{u}_{\alpha'})}\right\rangle \tag{29}$$

for the dimer centers of mass.

For the nematic ground state, when only the lowest-energy configuration is relevant, the structure factor is straightforwardly obtained as

$$S(\mathbf{q}) = S_0(\mathbf{q})f(\mathbf{q}), \tag{30}$$

where we have set

$$S_0(\mathbf{q}) = 2\,S_{\rm CM}(\mathbf{q})|_{T=0} = \frac{4}{N}\left[\sum_{\mathbf{R}} \cos(\mathbf{q}\cdot\mathbf{R})\right]^2 \tag{31}$$

and

$$f(\mathbf{q}) = \cos^2\left(\frac{\mathbf{q}\cdot\boldsymbol{\eta}}{2}\right). \tag{32}$$

In the above expressions, $S_0(\mathbf{q})$ represents the structure factor of N particles, arranged as a crystal of pointlike dimers at the $N/2$ lattice sites $\mathbf{R}$. The information on the actual size and orientation of the dimers is instead conveyed by $f(\mathbf{q})$ via the vector $\boldsymbol{\eta}$ connecting the particles within the dimer. Its direction is determined by the nematic orientation angle ϑ. For the HCGEM4 model at hand, its size η coincides with the hard-core diameter δ. This length δ is much smaller than the lattice spacings so that the oscillation period of $f(\mathbf{q})$ in $\mathbf{q}$ space is much longer than that of $S_0(\mathbf{q})$. Hence, generally speaking, the effect of $f(\mathbf{q})$ is to introduce a slowly varying amplitude modulation on the top of $S_0(\mathbf{q})$.

In the following we focus on the nematic state of Fig. 5(c), with $\boldsymbol{\eta}$ aligned in the y direction: here $f(\mathbf{q})$ is a slow function of the q_y component only.

Figure 8 reports the structure factor evaluated along the q_x and q_y symmetry axes of the rectangular centered arrangement of Fig. 5(c) by means of MC simulations carried out at the extremely small $T = 10^{-7}\,\varepsilon/k_{\rm B}$ in a supercell with $M = 20$ (800 particles). The zero-temperature $S(\mathbf{q})$ of Eqs. (30) and (31) yields Bragg peaks at integer multiples of $4\pi/d'' = 8.8426\,R^{-1}$ along q_x and at integer multiples of $2\pi/[d'\cos(\alpha_0/2)] = 5.0883\,R^{-1}$ along q_y, in excellent agreement with simulation results. Along q_x, perpendicularly to the nematic direction, the $f(\mathbf{q})$ of Eq. (32) is identically equal to unity, and indeed the peaks exhibit constant height N, whereas along q_y the modulation due to $f(\mathbf{q})$ intervenes. The agreement of the peak heights with $N \times f(\boldsymbol{q})$ is also remarkable. This agreement suggests that the long-range order of the exact ground state extends to small nonzero temperature. However, the reader is warned that this long-range order may be an artifact of the finite simulation size, as discussed in Sec. VI.

Even in a crystalline state characterized by long-range order, thermal fluctuations affect the scaling of the Bragg peak heights with size. For example, Fig. 9 reports the strength S_1 of the first Bragg peak of $S(\boldsymbol{q})$, located at $\boldsymbol{q} = (8.8426\,R^{-1}, 0)$ for the temperatures $T = 10^{-7}$ and $10^{-3}\,\varepsilon/k_{\rm B}$ as a function of the number of particles N. At both temperatures, S_1 scales linearly with N, as expected for finite-size crystals. However, for $T \gtrsim 10^{-3}\varepsilon/k_{\rm B}$, the values of S_1 are visibly smaller than the corresponding values at $T \simeq 0$, suggesting a significant disorder. To distinguish between the disordering of the dimer orientation and that of the phonon displacements of the dimer centers of mass, Fig. 9 reports also the corresponding peak intensity in $S_{\rm CM}(\boldsymbol{q})$ [Eq. (29)] as a function of the simulations size. The intermediate value indicates that at this temperature both phonon displacements and dimer orientation disorder contribute to the peak attenuation.

Above the ground state, for increasing temperature, a naive inspection of the energy scales in this model allows us to

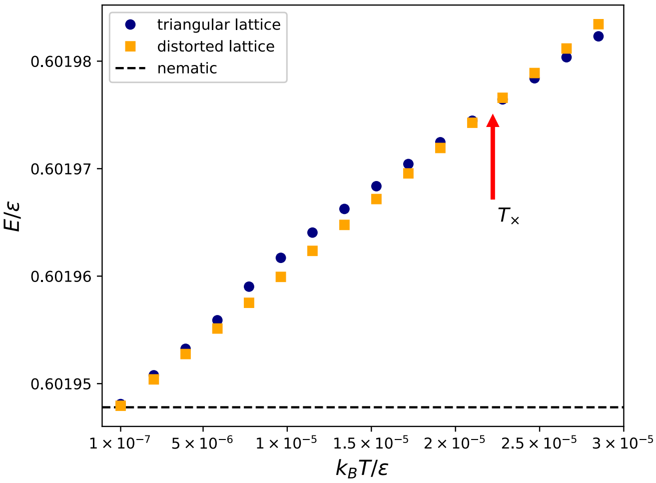

FIG. 10. The temperature dependence of the average energy per particle E, obtained by means of MC simulations in a supercell containing $N = 800$ particles. For $T > T_\times \simeq 2.25 \times 10^{-5}\varepsilon/k_B$ (marked by a red arrow), the energy corresponding to the triangular lattice (blue circles) turns lower than that of the centered-rectangular nematic state (orange squares), which prevails instead at low temperature. Error bars are smaller than the symbol size. The black dashed line marks the energy of the nematic ground state.

foresee (1) a nematic centered-rectangular state, followed by (2) a triangular dimer crystal with randomly fluctuating dimer orientations, which eventually melts into (3) a fluid state with no crystalline correlations.

To explore the thermal disordering of the nematic state, Fig. 10 shows the average energy per particle as a function of temperature up to $T \simeq 2.25 \times 10^{-5}\,\varepsilon/k_B$ (marked by the red arrow in the picture), comparing MC simulations carried out with periodic boundaries compatible either with the triangular lattice, or with the centered rectangular lattice obtained from the $T = 0$ minimizations. It is apparent that at low temperature the nematic centered rectangular geometry is more stable, while, starting from approximately $T = T_\times \simeq 2.25 \times 10^{-5}\,\varepsilon/k_B$ the orientationally disordered triangular geometry prevails. Note that $T_\times$ likely overestimates the actual temperature above which the nematic order is destabilized because the fixed cell geometry of the MC simulations does not allow for the actual self-consistent T-dependent lattice readjustment as the nematic order softens up.

This softening should also appear in the correlations between the orientations of the dimers, a feature to which $S(\boldsymbol{q})$ is not especially sensitive. To better characterize the thermal melting of the dimer-dimer correlations we evaluate the orientational correlation function

$$\langle\sigma_\alpha\sigma_{\alpha'}\rangle = \langle\cos[2(\theta_\alpha - \theta_{\alpha'})]\rangle, \tag{33}$$

following Ref. [41]. In the evaluation of this correlation function, we focus on the two crystalline directions, namely, along the x axis, indicated by $\langle\sigma_\alpha\sigma_{\alpha'}\rangle^x$, and along the "oblique" $\mathbf{e}_2$ lattice direction, indicated by $\langle\sigma_\alpha\sigma_{\alpha'}\rangle^o$. We report distances in units of lattice spacings $|\mathbf{e}_1| = d''$ and $|\mathbf{e}_2| = d'$, respectively.

We explore the temperature range between $T = 10^{-7}\,\varepsilon/k_\mathrm{B}$ and $T = 10^{-3}\,\varepsilon/k_\mathrm{B}$ where the nematic ordering of the dimers gives way to a orientationally disordered state. Figure 11 reports the simulation results for $\langle\sigma_\alpha\sigma_{\alpha'}\rangle^x$. Results for $\langle\sigma_\alpha\sigma_{\alpha'}\rangle^o$ are statistically compatible. At very low temperature ($T = 10^{-7}\,\varepsilon/k_\mathrm{B}$), $\langle\sigma_\alpha\sigma_{\alpha'}\rangle^x$ and $\langle\sigma_\alpha\sigma_{\alpha'}\rangle^o$ exhibit long-range correlations marked by their finite value even for the largest distances achievable, namely, half the simulation box side.

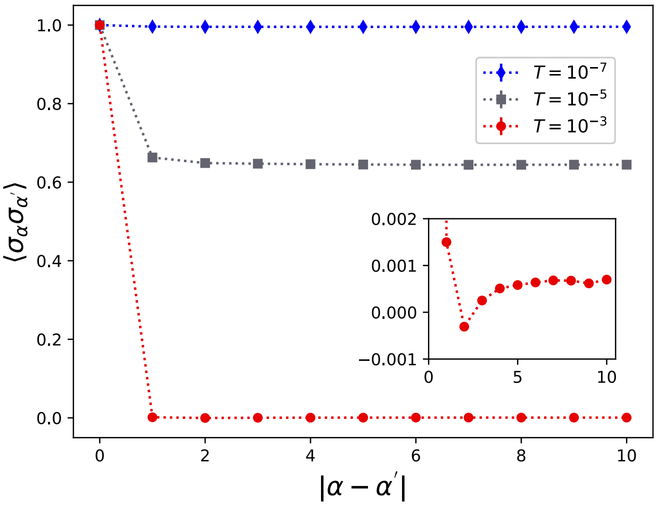

FIG. 11. The dimer-dimer angular correlation function $\langle\sigma_\alpha\sigma_{\alpha'}\rangle^x$, as obtained in simulations carried out at temperatures $T = 10^{-7}, 10^{-5}, 10^{-3}\,\varepsilon/k_\mathrm{B}$. The correlation function is expressed as a function of the dimer-dimer x separation $|\alpha - \alpha'|$ expressed in units of the lattice spacing d''. Error bars are smaller than the symbol size. Inset: zoom on the $T = 10^{-3}\,\varepsilon/k_\mathrm{B}$ data points.

On increasing the temperature, as exemplified, e.g., by the $T = 10^{-5}\,\varepsilon/k_\mathrm{B}$ data in Fig. 11, the system partially maintains a degree of ordering of the dimers, marked by the finite (albeit lower) value of $\langle\sigma_\alpha\sigma_{\alpha'}\rangle$ at large distance. This condition represents a crystalline state with a long-range nematic order reduced but not destroyed by fluctuations. At even higher temperatures (exemplified by $T = 10^{-3}\,\varepsilon/k_\mathrm{B}$ in Fig. 11), $\langle\sigma_\alpha\sigma_{\alpha'}\rangle^x$ is characterized instead by a rapid short-range decay of the correlations, corresponding to randomly disordered dimers. As evidenced in the inset of Fig. 11, at the highest reported temperature, $\langle\sigma_\alpha\sigma_{\alpha'}\rangle^x$ does not precisely vanish at large distance, but shows values in the order of 0.001. Note, however, that the simulations at all temperature are carried out in the supercell compatible with the centered rectangular lattice, which favors the dimer alignment along y, and consequent positive $\langle\sigma_\alpha\sigma_{\alpha'}\rangle^x$ correlations.

Even with their limited size, the simulations results help us to place an upper bound $T_\times$ to the temperature where dimer long-range orientational order is lost, and we can safely state that this bound is much lower than the transition temperature for the formation of a cluster solid. The latter can be estimated from the locus of divergence of the fluid structure factor in a mean-field approximation [22]—the so-called λ-line. For the regularized ($K = 5$) HCGEM4 potential at the density $\rho_2 = 1.13971\,R^{-2}$ considered here, this gives $T_\lambda \simeq 0.13\,\varepsilon/k_\mathrm{B}$, in semi-quantitative agreement with some additional simulations that we performed to this purpose, which locate the fluid-solid transition at $T \simeq 0.11\,\varepsilon/k_\mathrm{B}$. Hence, nematic ordering occurs at a temperature several orders of magnitude lower than that at which the dimer crystal forms.

B. The SCGL6 model

We identify the ground state of the SCGL6 interaction via gradient minimization of the potential energy per particle E along the lines sketched in Sec. III B. The initial nondimerized configurations with particles located at random positions inside the supercell evolve spontaneously to a dimerized state. For all initial starting points the lowest-energy configuration consists of just dimers, with neither isolated particles, nor clusters with $N_c > 2$. While this is far from surprising given that the value of ρ was chosen so as to favor dimer formation, it is nevertheless reassuring that such a behavior is recovered without enforcing it *a priori*. The dimers arrange into a nematic state with the same qualitative features as those of the ground state of the HCGEM4 potential described in Sec. V A and represented in Fig. 5: the centers of mass of the dimers are located at the sites of a centered rectangular lattice, resulting in the same kind of distortion as that discussed in Sec. III B for the SCGL6 potential. The equilateral triangles deform into isosceles ones with with two long sides of length $d' > d$ forming an angle α_0, and a short side of length $d'' < d$ orthogonal to the nematic axis. Even though each dimer is free to adopt its own optimal size, at equilibrium all dimers sizes η turn out identical.

Although the qualitative properties of the ground state are the same as those sketched in Fig. 5 for the HCGEM4 model, the structural parameters of the SCGL6 differ significantly. Specifically, the SCGL6 model has $d' = 1.54072\,R$, $d'' = 1.42690\,R$, $\alpha_0 = 55.170^\circ$, $90^\circ - \alpha_0 = 62.415^\circ$, $\eta = 0.31754\,R$. Clearly, compared to the HCGEM4 model, the SCGL6 model exhibits much bigger dimers, thus determining a more sizable coupling between the orientation and the lattice, which induces a larger amount of distortion relative to the triangular lattice.

The energy per particle of the nematic state just described amounts to $E = 1.10824438\,\varepsilon$. This state can be compared to the configuration reported in Fig. 5(a) of Ref. [20], which displays a portion of a state similar to that of Fig. 4, characterized by vortices induced by fixed boundary conditions incompatible with the centered-rectangular lattice that the model seeks to reach. The internal energy per particle of that state was $E = 1.108486\,\varepsilon$, slightly higher than the energy obtained here for the perfect nematic state: The difference is due to the energy cost (Fig. 7) of the same kind of vortex structure illustrated for the HCGEM4 model in Fig. 4.

VI. DISCUSSION AND CONCLUSION

In this paper we characterize the ground state of two similar 2D models for particles repelling each other through core-softened two-body potential-energy profiles. We focus on their dimerized phase, where the effective dimer-dimer repulsion favors a triangular lattice. The residual orientation-dependent dimer-dimer interactions favor an alignment of dimer pairs perpendicular to their joining direction. In the triangular lattice, this optimal alignment cannot be realized at all bonds. A nematic ground state resolves the frustration by coupling the dimer orientation to a crystalline-lattice anisotropy: The triangular lattice slightly deforms to a centered-rectangular lattice, characterized by a small shrinkage of the lattice spacing in the direction perpendicular to the nematic order. The resulting rows of more-closely spaced dimers fulfill the intra-row interaction perfectly; at the same time, the extra spacing between dimers of adjacent rows reduces the energy cost of the suboptimal interrow mutual alignment; see Fig. 5. Our findings agree qualitatively with those obtained in Refs. [14,15] for the ground state of the 2D square-shoulder fluid, where it was also pointed out that longer cluster size implies an higher degree of distortion of the lattice compared to the triangular case, again in agreement with our comparison between the HCGEM4 and SCGL6 potentials.

At finite temperature, this long-range ordered 2D ground state is challenged by thermal fluctuations. In the infinite-size limit, following Mermin's theorem [42], at any nonzero temperature one should expect no crystalline order. Therefore, strictly speaking, the long-range crystalline and nematic ground state cannot survive finite T, where the 2D system finds itself in a uniform (albeit strongly correlated) thermodynamic state. However, as the practical existence and stability of finite-temperature 2D crystals such as graphene suggests, the thermodynamic limit may not be appropriate to describe finite macroscopic systems [43]. In a macroscopically large but finite sample, the boundary conditions are most likely sufficient to stabilize an ordered crystalline phase, where the question about the effect of the thermal fluctuations on the dimer-dimer correlation functions is interesting.

According to our simulations, at low temperature $T < T_\times$, these models at large but finite size should exhibit the same nematic long-range order that characterizes their ground state. The nematic vector is expected to be reduced by thermal fluctuations, and likewise the crystalline anisotropy is also expected to decrease. Depending on the system size and boundaries, this ordered state is challenged by the formation of vortex and antivortex pairs such as those depicted in Fig. 4, leading to a Berezinskii-Kosterlitz-Thouless state [44,45], characterized by a power-law decay of the orientational correlation function $\langle \sigma_\alpha \sigma_{\alpha'} \rangle$ at large distance. At higher temperature $T \gtrsim T_\times$ this quasiordered state should leave space to an orientationally disordered state. Due to the dimers rotating randomly, the distorted centered rectangular lattice becomes unstable, so that the structure reverts back to the triangular lattice. Precisely due to this orientation-lattice coupling however, it is unclear whether the transition between the quasiordered state and the orientationally disordered one could still be classified as Berezinskii-Kosterlitz-Thouless [44,45] or its nature could be qualitatively different. The answer to this question involving correlation decays over extremely large scales is not accessible to our current simulation setup.

Core-softened interactions have been successfully employed to reproduce the nontriangular phases observed experimentally in colloidal particles at the air-water interface in the presence of microgels [4] or amphiphiles [5]. It then comes natural to ask whether there is any chance to observe in an experiment also the nematic orientational state predicted in this work. The experiments presented in Refs. [4,5] do correspond to the regime $k_\mathrm{B}T/\varepsilon \ll 1$. However, in order to explore the nematic state the temperatures would have to be several orders of magnitudes below the melting temperature of the dimer crystal, and this could be practically complicated in realistic setups. It is also true that the extra-small temperature estimation $T_\times \simeq 10^{-5}\,\varepsilon/k_\mathrm{B}$ for the HCGEM4 model is associated to the weak orientational coupling of the dimers, in turn the result of their small size. We predict that if smaller shell to core ratios, and thus wider dimers, were considered, as in the SCGL6 model, the nematic state could extend to significantly higher temperature, possibly bringing it within experimental reach.

A feature peculiar to the present model is that the anisotropy leading to a nematic order arises due to the spontaneous aggregation of particles, whose original interaction is isotropic. A similar nematic order is favored also in the different scenario where anisotropy is present from the very beginning, e.g., for repulsive potentials which are not spherically symmetric, but exhibit an additional dependence on the particle orientation appropriate to model the interaction between elliptical or rod-shaped objects. A nematic phase is indeed the well-established favored configuration of sufficiently dense and elongated rods [46,47].

Other interesting aspects, partly addressed for the square-shoulder case [14–17] but worth investigating in smooth soft-shell potentials, include (1) the quantitative dependence of the lattice properties on the dimer size, (2) the frustration of the dimer-dimer interaction and the resulting ground state in three dimensions, and (3) the determination, in both two and three dimensions, of the mutual arrangement of the larger clusters that occur in the phase diagram at higher density.

The coupling between orientational order and lattice distortion is an especially interesting aspect of the systems considered here. Exploring its effects on the isotropic-nematic transition by a detailed investigation of the system at finite temperature looks like an intriguing future development of this study.

ACKNOWLEDGMENTS

This work benefits from useful discussion with L. Consonni, L. Reatto, M. Rossini, and V. Tateo. We acknowledge the CINECA Agreement with the Università degli Studi di Milano (2017-2018 and 2019-2020), the CINECA Grants No. IscraB_PANDA (2019) and No. IscraC_SOFT-ONE (2018), and INDACO-UNITECH for providing high-performance computing resources and support. N.M. acknowledges support from Grant No. PRIN2017 UTFROM of the Italian Ministry of University and Research. D.P. acknowledges support from the Università degli Studi di Milano, Project No. PSR2019_DIP_008-Linea 2.

APPENDIX: DETAILS OF THE MINIMIZATION ALGORITHM

We perform the minimization of the potential energy per particle E of Eq. (16) by means of a preconditioned conjugate algorithm with adaptive stepsize. The variables ϑ_α, $s_{\alpha j}$, b_j, $\alpha = 1, \dots, n$, $j = 1, 2$, are determined recursively via the expressions

$$\vartheta_\alpha^{\,l+1} = \vartheta_\alpha^{\,l} - \lambda_l\, \bar{\zeta}_\alpha^{\,l}, \tag{A1}$$

$$s_{\alpha j}^{l+1} = s_{\alpha j}^{l} - \mu_l\, \bar{\xi}_{\alpha j}^{\,l}, \tag{A2}$$

$$b_j^{l+1} = b_j^{l} - \nu_l\, \bar{\chi}_j^{\,l}, \tag{A3}$$

where the index l refers to the iteration stage, λ_l, μ_l, ν_l give the size of the minimization steps, and $\bar{\zeta}_\alpha^{\,l}$, $\bar{\xi}_{\alpha j}^{\,l}$, $\bar{\chi}_j^{\,l}$ give the directions of descent. In the simple steepest descent of Eq. (19), these coincide with the gradients of E with respect to the above variables. In the present algorithm, they are determined as follows: we first introduce preconditioning by replacing the gradients with the quantities

$$\zeta_\alpha^{\,l} = \frac{\partial E}{\partial \vartheta_\alpha}\left(\frac{\partial^2 E}{\partial \vartheta_\alpha^2}\right)^{-1}\Bigg|_l, \tag{A4}$$

$$\xi_{\alpha j}^{\,l} = \frac{\partial E}{\partial s_{\alpha j}}\left(\frac{\partial^2 E}{\partial s_{\alpha j}^2}\right)^{-1}\Bigg|_l, \tag{A5}$$

$$\chi_j^{\,l} = \frac{\partial E}{\partial b_j}\left(\frac{\partial^2 E}{\partial b_j^2}\right)^{-1}\Bigg|_l, \tag{A6}$$

and then obtain the conjugate directions $\bar{\zeta}_\alpha^{\,l}$, $\bar{\xi}_{\alpha j}^{\,l}$, $\bar{\chi}_j^{\,l}$ by the recurrence relations

$$\bar{\zeta}_\alpha^{\,l} = \zeta_\alpha^{\,l} + \gamma_l\, \bar{\zeta}_\alpha^{\,l-1}, \tag{A7}$$

$$\gamma_l = \frac{\sum_\alpha \left(\zeta_\alpha^{\,l} - \zeta_\alpha^{\,l-1}\right)}{\sum_\alpha \left(\zeta_\alpha^{\,l-1}\right)^2}, \tag{A8}$$

$$\bar{\xi}_{\alpha j}^{\,l} = \xi_{\alpha j}^{\,l} + \tau_l\, \bar{\xi}_{\alpha j}^{\,l-1}, \tag{A9}$$

$$\tau_l = \frac{\sum_{\alpha,j} \left(\xi_{\alpha j}^{\,l} - \xi_{\alpha j}^{\,l-1}\right)}{\sum_{\alpha,j} \left(\xi_{\alpha j}^{\,l-1}\right)^2}, \tag{A10}$$

$$\bar{\chi}_j^{\,l} = \chi_j^{\,l} + \omega_l\, \bar{\chi}_j^{\,l-1}, \tag{A11}$$

$$\omega_l = \frac{\sum_j \left(\chi_j^{\,l} - \chi_j^{\,l-1}\right)}{\sum_j \left(\chi_j^{\,l-1}\right)^2}. \tag{A12}$$

In order to improve the robustness of the algorithm, every $\mathcal{N} = 100$ iterations (typically), the nonconjugate directions $\zeta_\alpha^{\,l}, \xi_{\alpha j}^{\,l}, \chi_j^{\,l}$ are used in Eqs. (A1)–(A3) instead of the conjugate ones. We verify convergence by means of the quantity Δ defined as

$$\Delta = \frac{1}{n}\sum_\alpha \left|\frac{\partial E^*}{\partial \vartheta_\alpha}\right| + \frac{1}{2n}\sum_{\alpha,j}\left|\frac{\partial E^*}{\partial s_{\alpha j}}\right| + \sum_j \left|\frac{\partial E^*}{\partial b_j^*}\right|, \tag{A13}$$

where the asterisks refer to reduced quantities $E^* \equiv E/\varepsilon$, $b^* \equiv bR$. Iteration was stopped when Δ became smaller than 10^{-12}.

Special attention must be paid to the choice of the stepsize parameters λ_l, μ_l, ν_l, since they crucially affect the efficiency of the minimization. We employ two different prescriptions for this purpose. In both of them, we restrict E along the line determined at fixed $\vartheta_\alpha^{\,l}$, $s_{\alpha j}^{l}$, b_j^{l}, $\bar{\zeta}_\alpha^{\,l}$, $\bar{\xi}_{\alpha j}^{\,l}$, $\bar{\chi}_j^{\,l}$ by Eqs. (A1)–(A3) and regard it as a function of λ, μ, ν by setting

$$f_l(\lambda, \mu, \nu) = E\big(\vartheta_\alpha^{\,l} - \lambda\, \bar{\zeta}_\alpha^{\,l}, s_{\alpha j}^{l} - \mu\, \bar{\xi}_{\alpha j}^{\,l}, b_j^{l} - \nu\, \bar{\chi}_j^{\,l}\big). \tag{A14}$$

According to the first prescription, the parameters λ_l, μ_l, ν_l are determined by minimizing $f_l(\lambda, \mu, \nu)$ with respect to each of its variables, while keeping the other two fixed. The minimization is performed by Brent's method [36]. In the second prescription, we regard again $f_l(\lambda, \mu, \nu)$ as a function of a single variable at fixed values of the other two, and set off to minimize it by solving the equations $\partial f_l/\partial\lambda=0$, $\partial f_l/\partial\mu=0$, $\partial f_l/\partial\nu=0$ via the Raphson-Newton method [36]. However, instead of iterating the procedure until convergence, we stop at the first Raphson-Newton step by setting

$$\lambda_l = -\frac{\partial f_l}{\partial\lambda}\left(\frac{\partial^2 f_l}{\partial\lambda^2}\right)^{-1}\Bigg|_{\lambda,\mu,\nu=0}, \tag{A15}$$

$$\mu_l = -\frac{\partial f_l}{\partial\mu}\left(\frac{\partial^2 f_l}{\partial\mu^2}\right)^{-1}\Bigg|_{\lambda,\mu,\nu=0}, \tag{A16}$$

$$\nu_l = -\frac{\partial f_l}{\partial\nu}\left(\frac{\partial^2 f_l}{\partial\nu^2}\right)^{-1}\Bigg|_{\lambda,\mu,\nu=0}. \tag{A17}$$

The derivatives of f_l with respect to λ, μ, ν are given by

$$\frac{\partial f_l}{\partial\lambda} = -\sum_{\beta}\frac{\partial E}{\partial\vartheta_\beta}\bigg|_l \bar{\zeta}_\beta^{\,l}, \tag{A18}$$

$$\frac{\partial^2 f_l}{\partial\lambda^2} = \sum_{\beta,\gamma}\frac{\partial^2 E}{\partial\vartheta_\beta\partial\vartheta_\gamma}\bigg|_l \bar{\zeta}_\beta^{\,l}\bar{\zeta}_\gamma^{\,l}, \tag{A19}$$

$$\frac{\partial f_l}{\partial\mu} = -\sum_{\beta,j}\frac{\partial E}{\partial s_{\beta j}}\bigg|_l \bar{\xi}_{\beta j}^{\,l}, \tag{A20}$$

$$\frac{\partial^2 f_l}{\partial\mu^2} = \sum_{\beta,\gamma,i,j}\frac{\partial^2 E}{\partial s_{\beta i}\partial s_{\gamma j}}\bigg|_l \bar{\xi}_{\beta i}^{\,l}\bar{\xi}_{\gamma j}^{\,l}, \tag{A21}$$

$$\frac{\partial f_l}{\partial\nu} = -\sum_{j}\frac{\partial E}{\partial b_j}\bigg|_l \bar{\chi}_j^{\,l}, \tag{A22}$$

$$\frac{\partial^2 f_l}{\partial\nu^2} = \sum_{i,j}\frac{\partial^2 E}{\partial b_i\partial b_j}\bigg|_l \bar{\chi}_i^{\,l}\bar{\chi}_j^{\,l}. \tag{A23}$$

For the minimization with respect to ϑ_α and $s_{\alpha j}$, we find it best to determine λ_l and μ_l starting with Brent's method, and switching to Raphson-Newton when convergence had been nearly achieved to polish up the result. For the parameter ν_l needed in the minimization with respect to b_j, Raphson-Newton is employed throughout. When using Raphson-Newton, one has to take into account that, since the potential energy is not a globally convex function of ϑ_α, $s_{\alpha j}$, b_j, it may occur that at some iteration stage Eqs. (A15)–(A23) lead to a negative value of λ_l, μ_l, or ν_l. In that case, the actual stepsize parameter is reset at some fixed positive value.

Moreover, while ϑ_α and $s_{\alpha j}$ are restricted to the intervals $[0,\pi)$ and [0,1) respectively, this requirement is not necessarily enforced by Eqs. (A1) and (A2). Since E is a periodic function of both variables, ϑ_α and $s_{\alpha j}$ are mapped back into the above intervals whenever necessary.

Equations (A4)–(A6) and (A18)–(A23) require the first and second derivatives of E with respect to ϑ_α, $s_{\alpha j}$, b_j, whose expressions we provide below. To this end, we rewrite Eq. (16)

$$E = \frac{1}{4n\nu}\sum_{\mathbf{G}}\widetilde{w}(G)F(\{\mathbf{r}_{\alpha\sigma}\},\mathbf{G}) - \frac{1}{2}w(0), \tag{A24}$$

where we have set

$$F(\{\mathbf{r}_{\alpha\sigma}\},\mathbf{G}) = \Big|\sum_{\alpha\sigma}e^{-i\mathbf{G}\cdot\mathbf{r}_{\alpha\sigma}}\Big|^2. \tag{A25}$$

Using Eq. (18), one obtains the square modulus of the reciprocal-lattice vector $\mathbf{G}=\mathbf{B}\cdot\mathbf{m}$,

$$G^2 = m_1^2b_1^2 + \left(m_1b_2 + m_2\frac{p}{b_1}\right)^2, \tag{A26}$$

where m_1 and m_2 are integers. Similarly, by performing the matrix product in Eq. (17) we obtain

$$\mathbf{G}\cdot\mathbf{r}_{\alpha\sigma} = 2\pi\,\mathbf{m}\cdot\mathbf{s}_\alpha + \bigg[m_1(b_1\cos\vartheta_\alpha + b_2\sin\vartheta_\alpha) + m_2\frac{p}{b_1}\sin\vartheta_\alpha\bigg]\frac{\eta}{2}\sigma. \tag{A27}$$

The dependence of E on ϑ_α and $\mathbf{s}_\alpha$ occurs uniquely through the Bragg diffraction factor $F(\{\mathbf{r}_\alpha\},\mathbf{G})$, so one has

$$\frac{\partial E}{\partial\vartheta_\beta} = \frac{1}{4n\nu}\sum_{\mathbf{G}}\widetilde{w}(G)\frac{\partial F(\{\mathbf{r}_{\alpha\sigma}\},\mathbf{G})}{\partial\vartheta_\beta}, \tag{A28}$$

$$\frac{\partial E}{\partial s_{\beta i}} = \frac{1}{4n\nu}\sum_{\mathbf{G}}\widetilde{w}(G)\frac{\partial F(\{\mathbf{r}_{\alpha\sigma}\},\mathbf{G})}{\partial s_{\beta i}}. \tag{A29}$$

The quantities b_i that identify the reciprocal lattice according to Eq. (18), on the other hand, appear via $\mathbf{G}$ both in $\widetilde{w}(G)$ and in $F(\{\mathbf{r}_\alpha\},\mathbf{G})$. Hence

$$\frac{\partial E}{\partial b_i} = \frac{1}{4n\nu}\sum_{\mathbf{G}}\bigg[\frac{\partial\widetilde{w}(G)}{\partial b_i}F(\{\mathbf{r}_\alpha\},\mathbf{G}) + \widetilde{w}(G)\frac{\partial F(\{\mathbf{r}_{\alpha\sigma}\},\mathbf{G})}{\partial b_i}\bigg]. \tag{A30}$$

The second derivatives $\partial^2E/(\partial\vartheta_\beta\partial\vartheta_\gamma)$, $\partial^2E/(\partial s_{\beta i}\partial s_{\gamma j})$, $\partial^2E/(\partial b_i\partial b_j)$ are immediately obtained from Eqs. (A28)–(A30) by further differentiation. The derivatives of $F(\{\mathbf{r}_\alpha\},\mathbf{G})$ needed in the above expressions are determined via Eq. (A25). By omitting the explicit dependence of F on the variables $\mathbf{r}_\alpha$, $\mathbf{G}$ for the sake of brevity, we obtain

$$\frac{\partial F}{\partial\vartheta_\beta} = 2\,\frac{\partial\,\mathbf{G}\cdot\mathbf{r}_{\beta1}}{\partial\vartheta_\beta}\sum_{\alpha,\sigma,\sigma'}\sigma'\sin[\,\mathbf{G}\cdot(\mathbf{r}_{\alpha\sigma}-\mathbf{r}_{\beta\sigma'})\,], \tag{A31}$$

$$\frac{\partial^2 F}{\partial\vartheta_\beta\partial\vartheta_\gamma} = 2\,\delta_{\beta\gamma}\frac{\partial^2\,\mathbf{G}\cdot\mathbf{r}_{\beta1}}{\partial\vartheta_\beta^2}\sum_{\alpha,\sigma,\sigma'}\sigma'\sin[\mathbf{G}\cdot(\mathbf{r}_{\alpha\sigma}-\mathbf{r}_{\beta\sigma'})] + 2\,\frac{\partial\,\mathbf{G}\cdot\mathbf{r}_{\beta1}}{\partial\vartheta_\beta}\,\frac{\partial\,\mathbf{G}\cdot\mathbf{r}_{\gamma_1}}{\partial\vartheta_\gamma} \times\left\{\sum_{\sigma,\sigma'}\sigma\sigma'\cos[\mathbf{G}\cdot(\mathbf{r}_{\beta\sigma}-\mathbf{r}_{\gamma\sigma'})] - \delta_{\beta\gamma}\sum_{\alpha,\sigma,\sigma'}\cos[\mathbf{G}\cdot(\mathbf{r}_{\alpha\sigma}-r_{\beta\sigma'})]\right\}, \tag{A32}$$

$$\frac{\partial F}{\partial s_{\beta i}} = 4\pi m_i \sum_{\alpha,\sigma,\sigma'} \sin[\,\mathbf{G}\cdot(\mathbf{r}_{\alpha\sigma} - r_{\beta\sigma'})\,], \tag{A33}$$

$$\frac{\partial^2 F}{\partial s_{\beta i}\partial s_{\gamma j}} = 8\pi^2 m_i m_j \left\{ \sum_{\sigma,\sigma'} \cos[\mathbf{G}\cdot(r_{\beta\sigma} - r_{\gamma\sigma'})] - \delta_{\beta\gamma} \sum_{\alpha,\sigma,\sigma'} \cos[\mathbf{G}\cdot(\mathbf{r}_{\alpha\sigma} - r_{\beta\sigma'})] \right\}, \tag{A34}$$

$$\frac{\partial F}{\partial b_i} = 2 \sum_{\alpha,\beta,\sigma,\sigma'} \frac{\partial \mathbf{G}\cdot\mathbf{r}_{\alpha\sigma}}{\partial b_i} \sin[\mathbf{G}\cdot(\mathbf{r}_{\beta\sigma'} - \mathbf{r}_{\alpha\sigma})], \tag{A35}$$

$$\frac{\partial^2 F}{\partial b_i \partial b_j} = 2 \sum_{\alpha,\beta,\sigma,\sigma'} \left\{ \frac{\partial \mathbf{G}\cdot\mathbf{r}_{\alpha\sigma}}{\partial b_i} \left(\frac{\partial \mathbf{G}\cdot\mathbf{r}_{\beta\sigma'}}{\partial b_j} - \frac{\partial \mathbf{G}\cdot\mathbf{r}_{\alpha\sigma}}{\partial b_j} \right) \cos[\mathbf{G}\cdot(\mathbf{r}_{\beta\sigma'} - \mathbf{r}_{\alpha\sigma})] + \frac{\partial^2 \mathbf{G}\cdot\mathbf{r}_{\alpha\sigma}}{\partial b_i \partial b_j} \sin[(\mathbf{G}\cdot(\mathbf{r}_{\beta\sigma'} - \mathbf{r}_{\alpha\sigma})] \right\}. \tag{A36}$$

The derivatives of $\mathbf{G}\cdot\mathbf{r}_{\beta\sigma}$ with respect to ϑ_β and b_i which appear in Eqs. (A31), (A32), (A35), and (A36) are obtained straightforwardly from Eq. (A27), and the derivatives of $\widetilde{w}(G)$ with respect to b_i in Eq. (A30) are obtained via the chain rule $\partial\widetilde{w}(G)/\partial b_i = (d\widetilde{w}(G)/dG^2)(dG^2/db_i)$, with G^2 given by Eq. (A26).

The same conjugate gradient algorithm described in Eqs. (A1)–(A23) was used to minimize the real-space expression of E of Eq. (24) with respect to $s_{\alpha j}$ and a_j, $\alpha = 1, \dots, 2n$, $j = 1, 2$. In this case we omit to report the explicit expression of the first and second derivatives of E, since they are straightforward.

[1] N. W. Ashcroft and N. D. Mermin, *Solid State Physics* (Saunders College Publishing, Philadelphia, 1976).
[2] F. Baletto and R. Ferrando, Rev. Mod. Phys. **77**, 371 (2005).
[3] Y. Norizoe and T. Kawakatsu, Europhys. Lett. **72**, 583 (2005).
[4] M. Rey, A. D. Law, D. M. A. Buzza, and N. Vogel, J. Am. Chem. Soc. **139**, 17464 (2017).
[5] M. Rey, T. Yu, K. Bley, K. Landfester, D. M. A. Buzza, and N. Vogel, Langmuir **34**, 9990 (2018).
[6] V. S. K. Balagurusamy. G. Ungar, V. Perec, and G. Johansson, J. Am. Chem. Soc. **119**, 1539 (1997).
[7] G. A. McConnell and A. P. Gast, Phys. Rev. E **54**, 5447 (1996).
[8] G. A. McConnell and A. P. Gast, Macromolecules **30**, 435 (1997).
[9] S. Fischer and A. Exner, Proc. Natl. Acad. Sci. USA **108**, 1810 (2011).
[10] G. Malescio and G. Pellicane, Nat. Mater. **2**, 97 (2003).
[11] G. Malescio and G. Pellicane, Phys. Rev. E **70**, 021202 (2004).
[12] E. A. Jagla, J. Chem. Phys. **110**, 451 (1999).
[13] E. A. Jagla, Phys. Rev. E **58**, 1478 (1998).
[14] J. Fornleitner and G. Kahl, Europhys. Lett. **82**, 18001 (2008).
[15] J. Fornleitner and G. Kahl, J. Phys.: Condens. Matter **22**, 104118 (2010).
[16] G. J. Pauschenwein and G. Kahl, Soft Matter **4**, 1396 (2008).
[17] G. J. Pauschenwein and G. Kahl, J. Chem. Phys. **129**, 174107 (2008).
[18] W. R. C. Somerville, A. D. Law, M. Rey, N. Vogel, A. J. Archer, and D. M. A. Buzza, Soft Matter **16**, 3564 (2020).
[19] B. M. Mladek, P. Charbonneau, C. N. Likos, D. Frenkel, and G. Kahl, J. Phys.: Condens. Matter **20**, 494245 (2008).
[20] M. Rossini, L. Consonni, A. Stenco, L. Reatto, and N. Manini, Phys. Rev. E **97**, 052614 (2018).
[21] B. M. Mladek, D. Gottwald, G. Kahl, M. Neumann, and C. N. Likos, Phys. Rev. Lett. **96**, 045701 (2006); **97**, 019901(E) (2006).
[22] C. N. Likos, B. M. Mladek, D. Gottwald, and G. Kahl, J. Chem. Phys. **126**, 224502 (2007).
[23] S. Prestipino and F. Saija, J. Chem. Phys. **141**, 184502 (2014).
[24] R. Diaz-Mendez, F. Mezzacapo, F. Cinti, W. Lechner, and G. Pupillo, Phys. Rev. E **92**, 052307 (2015).
[25] C. N. Likos, A. Lang, M. Watzlawek, and H. Löwen, Phys. Rev. E **63**, 031206 (2001).
[26] F. Mambretti, S. Molinelli, D. Pini, G. Bertaina, and D. E. Galli, Phys. Rev. E **102**, 042134 (2020)
[27] S. Rossotti, M. Teruzzi, D. Pini, D. E. Galli, and G. Bertaina, Phys. Rev. Lett. **119**, 215301 (2017).
[28] S. Prestipino, A. Sergi, and E. Bruno, J. Phys. A: Math. Theor. **52**, 015002 (2019).
[29] A. Imperio and L. Reatto, J. Phys.: Condens. Matter **16**, S2769 (2004); J. Chem. Phys. **124**, 164712 (2006).
[30] A. J. Archer, Phys. Rev. E **78**, 031402 (2008).
[31] D. Pini and A. Parola, Soft Matter **13**, 9259 (2017).
[32] D. Pini, Soft Matter **14**, 6595 (2018).
[33] T. Neuhaus and C. N. Likos, J. Phys.: Condens. Matter **23**, 234112 (2011).
[34] S. Prestipino, D. Gazzillo, and N. Tasinato, Phys. Rev. E **92**, 022138 (2015).
[35] D. Pini, A. Parola, and L. Reatto, J. Chem. Phys. **143**, 034902 (2015).
[36] W. H. Press, S. A. Teukolsky, W. T. Vetterling, and B. P. Flannery, *Numerical Recipes*, 2nd ed. (Cambridge University Press, Cambridge, 1992).
[37] S. Kirkpatrick, C. D. Gelatt, Jr., and M. P. Vecchi, Science **4598**, 671 (1983).
[38] N. Metropolis, A. W. Rosenbluth, M. N. Rosenbluth, A. H. Teller, and E. Teller, J. Chem. Phys. **21**, 1087 (1953).
[39] https://github.com/francescomambretti/soft_2D_classical_dimers.

[40] D. A. Kofke, J. Chem. Phys. **117**, 6911 (2002).
[41] G. Watanabe, J. I. Saito, N. Kato, and Y. Tabe, J. Chem. Phys. **134**, 054513 (2011).
[42] N. D. Mermin, Phys. Rev. **176**, 250 (1968).
[43] R. C. Thompson-Flagg, M. J. B. Moura, and M. Marder, Europhys. Lett. **85**, 46002 (2009).
[44] J. M. Kosterlitz and D. J. Thouless, J. Phys. C: Solid State Phys. **6**, 1181 (1973).
[45] V. N. Ryzhov, E. E. Tareyeva, Yu. D. Fomin, and E. N. Tsiok, Phys.-Usp. **60**, 857 (2017).
[46] J. D. Parsons, Phys. Rev. A **19**, 1225 (1979).
[47] M. A. Bates and D. Frenkel, J. Chem. Phys. **112**, 10034 (2000).